Compressibility effects on energy exchange mechanisms in a spatially developing plane free shear layer

D. Li[1], A. Peyvan[1], Z. Ghiasi[1], J. Komperda[1] and F. Mashayek[1],†

[1]Department of Mechanical and Industrial Engineering, University of Illinois at Chicago, Chicago, IL 60607, USA

The compressibility effects on energy exchange mechanisms in a three-dimensional, spatially developing plane free shear layer are investigated via data produced by direct numerical simulation. The compressible shear layer is simulated using a high-order discontinuous spectral element method for convective Mach numbers $M_c = 0.3$, 0.5 and 0.7. The energy exchange mechanisms in the flow are examined by analysing the budget terms of mean kinetic, internal and turbulent kinetic energy transport equations, in both transition and turbulent regions. The results show that turbulent production, turbulent viscous dissipation, mean viscous dissipation, pressure dilatation and enthalpic production are the main mechanisms responsible for energy exchange among different forms of energy. The effects of compressibility on energy transfer mechanisms are studied based on the analyses of those five budget terms. The primary budget terms evolve differently in the transition and turbulent regions and change significantly for varying compressibility. In the transition region, a double-peak variation becomes a single peak in the streamwise profile of the turbulent production as M_c increases from 0.3 to 0.7, due to significant changes in the vortex pairing structures. The shear layer centre slightly shifts to the high-speed side due to the appearance of the velocity deficit. The velocity deficit presence distance (VDPD) becomes longer as compressibility increases. However, in the turbulent region, the cross-stream profiles of the main budget terms significantly shift to the low-speed side because of the asymmetric mass entrainment and shift even further as M_c increases.

Key words: compressible turbulence, free shear layers, flow–structure interactions

1. Introduction

Understanding the compressibility effects on energy exchange in turbulent plane shear layers can provide useful insights into the physical processes such as those involved in supersonic combustion and propulsion (Elliott & Samimy 1990; Lele 1994; Pope 2000). Turbulent energy exchange is achieved through two main mechanisms: energy exchange among turbulent kinetic energy (TKE), mean kinetic energy (MKE) and mean internal energy (MIE); and energy redistribution in space. These two mechanisms are often studied

† Email address for correspondence: mashayek@uic.edu

through the turbulent energy budgets. The compressibility effects on turbulent energy budgets are often examined in terms of the convective Mach number, $M_c = \Delta U/(c_1 + c_2)$ (Bogdanoff 1983). Here, $\Delta U = U_1 - U_2$, where U_1 and U_2 are the velocities of the high- and low-speed streams, respectively. Also, c_1 and c_2 are the speeds of sound on the high- and low-speed sides of the free shear layer (FSL), respectively.

The early studies on compressible flows were performed using linearized governing equations, or two-dimensional (2-D) direct numerical simulation (DNS), due to their low computational resource requirements (Kovasznay 1953; Chu & Kovasznay 1958; Passot & Pouquet 1987; Erlebacher *et al.* 1990). Kovasznay (1953) and Chu & Kovasznay (1958) conducted theoretical studies applying the linearized governing equations to identify the vorticity, acoustic and entropy modes in a compressible flow. Later, Passot & Pouquet (1987) carried out a 2-D DNS study for compressible turbulence. They found that the change in the turbulent viscous dissipation is related to the change of Mach number, and the energy exchange between the compressive components and internal energy is oscillating over time. Passot & Pouquet (1987) also suggested that shocks could produce shear turbulence in supersonic flows.

Due to the drawbacks of the 2-D turbulent simulation, such as unphysical turbulence, researchers tended to favour three-dimensional (3-D) compressible turbulent flows. Early 3-D DNS studies were performed for isotropic compressible turbulent flows (Kida & Orszag 1990, 1992). The authors decomposed the dissipation into solenoidal and dilatational dissipation components, and the pressure fluctuations into compressible and incompressible parts. Zeman (1990) suggested that the dilatational dissipation is a function of both the TKE and the turbulence Mach number. Sarkar *et al.* (1991*b*) and Sarkar & Lakshmanan (1991) concluded that the compressible dissipation and pressure dilatation need to be modelled in a compressible turbulent flow. Later, 3-D homogeneous compressible shear flows were utilized to investigate the compressibility effects on the flow properties (Chen, Cantwell & Mansour 1989; Sandham & Reynolds 1990; Sarkar, Erlebacher & Hussaini 1991*a*; Blaisdell, Mansour & Reynolds 1993; Sarkar 1995; Blaisdell, Coleman & Mansour 1996; Simone, Coleman & Cambon 1997; Hamba 1999). The authors discovered several compressibility effects on turbulent flows, such as the stabilization of the turbulent shear flow, the reduction in the growth rate of the shear layer, and the decrease in turbulent production and TKE. They also found that the ratio of the dilatational dissipation to solenoidal dissipation increases as the convective Mach number increases. Sarkar & Lakshmanan (1991) reported that the dilatation of the velocity field produces the pressure dilatation and the compressible dissipation, which facilitate the transfer of energy between kinetic and internal forms. Huang, Coleman & Bradshaw (1995) conducted DNS of temporally evolving compressible channel flows to investigate the effects of compressibility on turbulence energy budgets. The authors observed that the turbulent density and pressure fluctuation yield insignificant compressibility effects. The study by Day, Mansour & Reynolds (2001), on the compressible shear layer with heat release in a reacting flow, examined the effect of heat release and compressibility on the structure of the flow. Livescu, Jaberi & Madnia (2002) studied the effect of the heat release on the turbulent energy exchange in reacting, temporally evolving, homogeneous shear flow using DNS. They showed that the pressure dilatation transfers energy from the internal energy to the kinetic energy. The authors also found that the temporal growth rate of TKE is primarily influenced by the heat release through variations of pressure dilatation and dilatational-dissipation terms.

Foysi & Sarkar (2010) studied the effect of the compressibility on the evolution of the temporal mixing layer using large eddy simulation (LES). They reported that the impact of the compressibility on the pressure–strain correlation is significant.

Atoufi, Fathali & Lessani (2015) carried out LES of a temporally developing compressible mixing layer. The authors suggested that the pressure-dilatation term is responsible for transferring MIE into MKE, while the mean pressure-dilatation term transfers TKE into MIE. They also reported that the magnitude of the dynamic Smagorinsky model coefficient, the subgrid-scale dissipation of TKE, and the subgrid-scale pressure dilatation decrease with increasing convective Mach number.

According to the literature, in a spatially developing turbulent plane FSL with naturally developing inflow condition, the role played by compressibility on energy exchange is not fully understood. There are no available DNS data or studies for energy exchange among different forms of energy in such a flow for different convective Mach numbers. In this context, we investigate the energy exchange among TKE, MKE and MIE, and the compressibility effects on such energy transfer mechanisms using DNS with a high-order discontinuous spectral element method (DSEM) (Kopriva & Kolias 1996; Kopriva 1998; Jacobs, Kopriva & Mashayek 2005). This method has been used for DNS and LES of compressible flows (Li *et al.* 2016; Ghiasi *et al.* 2016, 2019; Li *et al.* 2019; Komperda *et al.* 2020b) as well as turbulent reacting flows (Komperda *et al.* 2020a). The two primary objectives of this work are: (i) to identify the energy exchange mechanisms responsible for energy exchange among TKE, MKE and MIE; (ii) to investigate the effects of compressibility on the energy exchange mechanisms. The remainder of this paper is organized as follows. First, the governing equations and the numerical methodology are briefly described. Then, we present and discuss the problem set-up and results of the simulations. Finally, we present a summary of significant findings.

2. Simulation details

2.1. *Governing equations*

The governing equations are the full Navier–Stokes equations and solved in conservative form. In non-dimensional form with Cartesian vector notation, they are expressed as (Jacobs, Kopriva & Mashayek 2004; Jacobs *et al.* 2005)

$$\frac{\partial \mathbf{Q}}{\partial t} + \frac{\partial \mathbf{F}_i^a}{\partial x_i} = \frac{1}{Re_f} \frac{\partial \mathbf{F}_i^v}{\partial x_i}, \tag{2.1}$$

where

$$\mathbf{Q} = \begin{pmatrix} \rho \\ \rho u_1 \\ \rho u_2 \\ \rho u_3 \\ \rho e \end{pmatrix}, \quad \mathbf{F}_i^a = \begin{pmatrix} \rho u_i \\ p\delta_{i1} + \rho u_1 u_i \\ p\delta_{i2} + \rho u_2 u_i \\ p\delta_{i3} + \rho u_3 u_i \\ u_i(\rho e + p) \end{pmatrix}, \quad \mathbf{F}_i^v = \begin{pmatrix} 0 \\ \sigma_{i1} \\ \sigma_{i2} \\ \sigma_{i3} \\ -q_i + u_k \sigma_{ik} \end{pmatrix}. \tag{2.2a–c}$$

Here, $\mathbf{Q}$, $\mathbf{F}_i^a$ and $\mathbf{F}_i^v$ are the solution, advective flux and viscous flux vectors, respectively. The total energy, heat flux vector, and viscous stress tensor are defined as

$$\rho e = \frac{p}{\gamma - 1} + \frac{1}{2}\rho u_k u_k, \tag{2.3}$$

$$q_i = -\frac{1}{(\gamma - 1) Pr_f M_f^2} \frac{\partial T}{\partial x_i}, \tag{2.4}$$

$$\sigma_{ik} = \frac{\partial u_i}{\partial x_k} + \frac{\partial u_k}{\partial x_i} - \frac{2}{3}\frac{\partial u_j}{\partial x_j}\delta_{ik}, \tag{2.5}$$

respectively. Here, p, γ, ρ, u, δ_{ij} and T are the pressure, specific heats ratio, density, velocity, Kronecker delta and temperature, respectively. The reference Reynolds number, reference Prandtl number and reference Mach number, are generated from non-dimensionalizing the Navier–Stokes equations, and are, respectively, defined as

$$Re_f = \frac{\rho_f^* U_f^* L_f^*}{\mu^*}, \quad Pr_f = \frac{\mu^* c_p^*}{\kappa^*}, \quad M_f = \frac{U_f^*}{\sqrt{\gamma R^* T_f^*}}, \qquad (2.6a\text{–}c)$$

where U, L, μ, c_p, κ and R are the velocity, length, dynamic viscosity, specific heat at constant pressure, thermal conductivity and gas constant, respectively. The superscript $*$ denotes dimensional quantities, and the subscript f indicates reference values. In this work, the dynamic viscosity, specific heat and thermal conductivity of the fluid are assumed to be independent of temperature because the temperature variations encountered in all cases are not significant ($<6\%$). The equation of state closes the aforementioned equations and is defined as

$$p = \frac{\rho T}{\gamma M_f^2}. \qquad (2.7)$$

2.2. *Numerical method*

In this study, we use the DSEM code as the compressible flow solver (Jacobs *et al.* 2004, 2005). The computational domain is partitioned into hexahedral elements. Each element is mapped onto a unit cube over the interval [0, 1] in each direction applying isoparametric mapping. After the mapping, (2.1) reads

$$\frac{\partial \tilde{Q}}{\partial t} + \frac{\partial \tilde{F}_i^a}{\partial X_i} = \frac{1}{Re_f} \frac{\partial \tilde{F}_i^v}{\partial X_i}, \qquad (2.8)$$

where

$$\tilde{Q} = JQ, \quad \tilde{F}_i^a = \frac{\partial X_i}{\partial x_j} F_j^a, \quad \tilde{F}_i^v = \frac{\partial X_i}{\partial x_j} F_j^v. \qquad (2.9a\text{–}c)$$

Here, the solution vector, Q and flux vectors, F, are in the physical space, while $\tilde{Q}$ and $\tilde{F}$ are in the mapped space, and J is the determinant of the Jacobian matrix of the isoparametric transformation (Jacobs 2003). The term, $\partial X_i / \partial x_j$, is the metrics matrix, where x_j and X_i denote the coordinates of the physical and mapped spaces, respectively.

In each element of the mapped space, high-order Lagrange basis functions approximate the solution values, $\tilde{Q}$, and the fluxes, $\tilde{F}_i$, (in (2.8)) on the Gauss quadrature points and Lobatto quadrature points, defined as

$$X_{j+1/2} = \frac{1}{2} \left\{ 1 - \cos \left[\frac{(2j+1)\pi}{2N} \right] \right\}, \quad j = 0, \dots, N-1 \qquad (2.10)$$

and

$$X_j = \frac{1}{2} \left\{ 1 - \cos \left[\frac{\pi j}{N} \right] \right\}, \quad j = 0, \dots, N, \qquad (2.11)$$

respectively, within the interval [0, 1]. Here, $N - 1$ indicates the polynomial order of the spectral element. The solution on the Gauss quadrature points is approximated as

$$\tilde{Q}(X, Y, Z) = \sum_{i=0}^{N-1} \sum_{j=0}^{N-1} \sum_{k=0}^{N-1} \tilde{Q}_{i+1/2, j+1/2, k+1/2} h_{i+1/2}(X) \, h_{j+1/2}(Y) \, h_{k+1/2}(Z). \qquad (2.12)$$
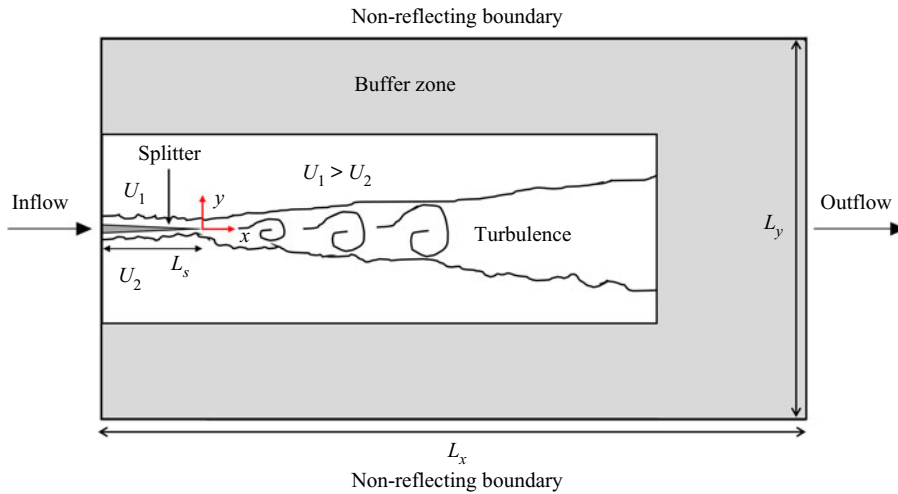
FIGURE 1. Schematic of the computational domain.

Here, X, Y and Z denote the mapped space coordinates, while $h_{j+1/2}$ indicates the Lagrange interpolating polynomial on the Gauss points. After computing the viscous and inviscid fluxes, a fourth-order low-storage Runge–Kutta scheme is utilized for time integration (Carpenter & Kennedy 1994).

2.3. *Simulation conditions*

The computational domain is bounded with inflow and outflow boundaries in the streamwise (x) direction (Jacobs, Kopriva & Mashayek 2003), non-reflecting boundaries in the cross-stream (y) direction (Thompson 1987, 1990; Poinsot & Lele 1992; Jacobs *et al.* 2003) and periodic boundaries in the spanwise (z) direction. To damp any high-wavenumber oscillations produced at the outlet boundary, a buffer zone near the boundary is adopted, and a damping-sponge is achieved by grid stretching. A schematic of such a domain is shown in figure 1. For the detailed description of the boundary conditions, we refer to our previous work (Li *et al.* 2019) – hereinafter referred to as 'part I'.

The necessary parameters are chosen to analyse the compressibility effects on the turbulent FSL. For all simulations, the free stream speeds at the high- and low-speed sides are specified to satisfy the ratio, $R = 0.54$, which is defined as

$$R = \frac{U_1 - U_2}{U_1 + U_2}. \tag{2.13}$$

The following computations employ both Reynolds and Favre averaging. Angled brackets, $\langle \rangle$, denote Reynolds average, while curly brackets, {}, indicate density-weighted (Favre) average. For any variable f, the Reynolds decomposition is defined as (Favre 1969)

$$f = \langle f \rangle + f', \tag{2.14}$$

where f' is the turbulent fluctuation with respect to Reynolds average denoted by the superscript $'$. The Reynolds average, $\langle f \rangle$, can be found from an average in time or an

M_c	R	ΔU	M_1	M_2	M_a	M_t	M_g	x_R	x_E
0.3	0.54	2.1	0.8556	0.2556	0.581	0.12	0.67	30	340
0.5	0.54	3.5	1.4259	0.4259	0.990	0.19	1.11	170	550
0.7	0.54	4.9	1.9963	0.5963	1.423	0.26	1.54	230	670

TABLE 1. Simulation parameters and approximated flow properties. Here $M_1 = U_1/c_1$ and $M_2 = U_2/c_2$ are the inflow Mach numbers; $M_a = \{u\}/c_0$, $M_t = \sqrt{k}/c_0$ and $M_g = Sl/c_0$ are the local Mach number, turbulent Mach number and gradient Mach number, respectively, evaluated at the centreline of the FSL in turbulent region; k is the TKE; S is the mean shear rate in the cross-stream direction; l is the integral length scale of the streamwise velocity in the shear direction; $c_0 = (c_1 + c_2)/2$ is the mean speed of sound; x_R is the location where the roll-up of vortex sheet originates, while x_E indicates the location where the transition completes (see part I for more detail).

ensemble average in space. Similarly, the Favre decomposition is defined as (Favre 1969)

$$f = \{f\} + f'', \tag{2.15}$$

where f'' is the turbulent fluctuation from Favre average indicated by the superscript $''$. The Favre average, $\{f\}$ can be computed by

$$\{f\} = \langle \rho f \rangle / \langle \rho \rangle. \tag{2.16}$$

The role of compressibility in the FSL flow can be expressed in terms of the convective Mach number, M_c, for the flow with the same specific heat ratios (Bogdanoff 1983). Three simulations are carried out for three different convective Mach numbers and inflow Mach numbers, which are presented in table 1. The inflow Mach numbers of the high- and low-speed sides of the shear layer are denoted by $M_1 = U_1/c_1$ and $M_2 = U_2/c_2$, respectively. Besides the convective Mach number, we also estimate the roles of the local Mach number, M_a, gradient Mach number, M_g, and turbulent Mach number, M_t (Sarkar 1995; Pantano & Sarkar 2002) in the conducted cases. The local Mach number, $M_a = \{u\}/c_0$, is based on the mean streamwise velocity, $\{u\}$; the gradient Mach number, $M_g = Sl/c_0$, is determined by mean velocity gradient, $S = \mathrm{d}\{u\}/\mathrm{d}y$, and the integral length scale in the shear direction, l; the turbulent Mach number, $M_t = \sqrt{k}/c_0$, is based on the TKE, k (Sarkar 1995). The mean speed of sound is $c_0 = (c_1 + c_2)/2$.

The M_a and M_g are similar to M_c in the sense that they are determined by the mean velocity field. The M_a is the ratio of mean velocity ($\{u\}$) to the speed of sound (c_0). The M_g can be viewed as a ratio of the mean velocity difference (Sl) across a large eddy to the speed of sound (Sarkar 1995). The M_c is determined by the ratio of the mean velocity difference between two free streams (ΔU) in an FSL to the speed of sound. However, M_g and M_t have key differences with respect to M_c. The M_g and M_t are field quantities, which vary across an inhomogeneous FSL. Moreover, the M_t is based on the velocity fluctuation field, unlike M_c.

The maximum values of M_g and M_t are located along the centreline of the shear layer since the centreline has the largest mean velocity gradient S and TKE k in the cross-stream direction. In contrast, the maximum value of the local Mach number M_a appears in the high-speed free stream, which equals M_1. The value of M_a then gradually decreases across the shear layer until reaching a minimum value of M_2 in the low-speed side. Figure 2 presents a comparison of the values of M_a, M_g and M_t at $x - x_E = 300$ at the centreline of
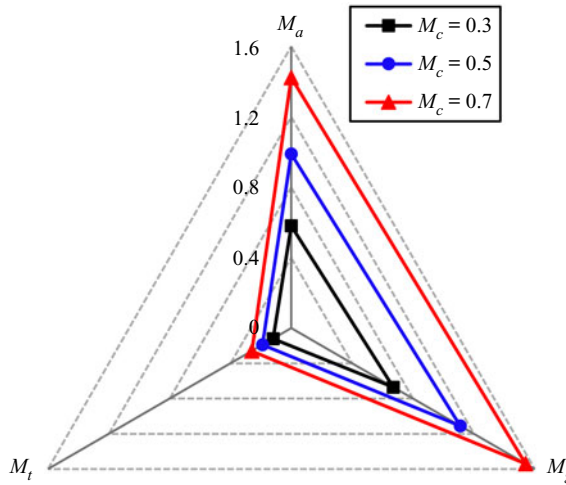
FIGURE 2. Comparison of M_a, M_g and M_t at $x - x_E = 300$ at the centre of the shear layer for $M_c = 0.3$, 0.5 and 0.7.

the shear layer for $M_c = 0.3$, 0.5 and 0.7. The corresponding values are also tabulated in table 1. The x_E is defined in the caption of table 1. Figure 2 shows that for each case, the values of M_a and M_g are nearly two times of the corresponding M_c, while the value of M_t is approximately 40 % of the corresponding M_c. It is important to note that the values of M_a, M_g and M_t are proportional to the corresponding M_c at the centreline of the shear layer in the turbulent region (also see table 1). Hence, based on these considerations, the difference of using M_c, M_a, M_g and M_t to interpret the role of compressibility at the centreline of the shear layer is expected to be small. However, for the area near the edges of the shear layer (the high- and low-speed edges), there is a significant differentiation between using M_c and other Mach numbers (e.g. the values of M_g and M_t are close to zero). In conclusion, M_c may better suit a spatially developing FSL than other Mach numbers for representing the role of compressibility.

The momentum thickness Reynolds number, Re_θ, based on ΔU and $\delta_{\theta 1}$, is chosen as 140, since it is large enough for transition to turbulence and small enough for resolving the flow. Here, $\delta_{\theta 1}$ is the initial momentum thickness of the upper boundary layer (high-speed side), and is evaluated just upstream of the trailing edge. The momentum thickness of a spatially developing compressible plane FSL is defined as (Jiménez 2004)

$$\delta_\theta = \frac{1}{\rho_o} \int_{-\infty}^{+\infty} \langle \rho \rangle \frac{\{u\} - U_2}{\Delta U} \left(1 - \frac{\{u\} - U_2}{\Delta U} \right) \mathrm{d}y, \tag{2.17}$$

where ρ_o denotes the initial inflow density. The microscale Reynolds number is defined as (Tennekes & Lumley 1972)

$$Re_\lambda = 2k \sqrt{\frac{5}{\nu \varepsilon}}, \tag{2.18}$$

where ν and ε are kinematic viscosity and turbulent viscous dissipation, respectively. The values of Re_λ are presented in table 2, evaluated at the centreline of the shear layer in the self-similar turbulent region. Other parameters are the ratio of specific heats $\gamma = 1.4$ and the reference Prandtl number $Pr_f = 0.7$.

M_c	$\dfrac{\mathrm{d}\delta_\theta}{\mathrm{d}x}$	Re_λ	$\dfrac{L_\eta}{\Delta x_{ave}}$	$\dfrac{L_\eta}{\Delta x_{min}}$	$\dfrac{L_\eta}{\Delta x_{max}}$	$\dfrac{L_\eta}{\Delta y_{ave}}$	$\dfrac{L_\eta}{\Delta y_{min}}$	$\dfrac{L_\eta}{\Delta y_{max}}$	$\dfrac{L_\eta}{\Delta z_{ave}}$	$\dfrac{L_\eta}{\Delta z_{min}}$	$\dfrac{L_\eta}{\Delta z_{max}}$
0.3	0.0137	184	0.458	4.665	0.298	0.398	3.854	0.258	0.489	4.835	0.316
0.5	0.0121	216	0.487	4.958	0.317	0.423	4.096	0.275	0.519	5.138	0.336
0.7	0.0106	208	0.484	4.929	0.315	0.421	4.072	0.273	0.516	5.108	0.334

TABLE 2. Values of parameters for the cases with $M_c = 0.3$, 0.5 and 0.7 evaluated at the centreline of the shear layer in the self-similar turbulent region. Here $\mathrm{d}\delta_\theta/\mathrm{d}x$ is the momentum thickness growth rate.

2.4. *Computational domain and grid*

All dimensions of the computational domain are normalized by the initial shear layer momentum thickness, $\delta_{\theta 1}$. The size of the domain for each case is set to $L_x \times L_y \times L_z = 1982 \times 1600 \times 140$. The subscripts x, y and z denote the streamwise, cross-stream and spanwise directions, respectively. The region of interest for all cases is $0 \leqslant x \leqslant 1300$, which is used for studying the properties of the compressible FSL. The rest of the domain is employed as a large buffer zone to prevent solution contamination from the outlet boundary (see figure 1). A detailed description of the computational domain is reported in part I. A non-uniform grid distribution is utilized to fulfil a finer grid in the FSL. For $x \leqslant 1300$, the grid in the x-direction attains an average spacing $\Delta x_{ave} = 0.580$ with a minimum spacing $\Delta x_{min} = 0.057$ and a maximum spacing $\Delta x_{max} = 0.892$ due to the non-uniform nature of the Chebyshev grid used in this study. The average vertical grid size is $\Delta y_{ave} = 0.668$ in the shear layer area while the minimum and maximum vertical grid sizes reach $\Delta y_{min} = 0.069$ and $\Delta y_{max} = 1.029$. The 2-D element grid on the x–y plane is uniformly extruded in the spanwise direction to construct a 3-D grid. The average spanwise grid size is $\Delta z_{ave} = 0.544$, and the minimum and maximum are $\Delta z_{min} = 0.055$ and $\Delta z_{max} = 0.841$, respectively. The evaluated ratios of the Kolmogorov scales to grid sizes for all three cases are listed in table 2, where the Kolmogorov scale, L_η, is defined as (Landahl & Mollo-Christensen 1992)

$$L_\eta = (\nu^3/\varepsilon)^{0.25}. \tag{2.19}$$

The average grid size is slightly smaller than that used by Pantano & Sarkar (2002) in their DNS study of a periodic shear flow. In this work, the grid consists of 1 368 260 elements. A polynomial order of five is used resulting in a total of 295 544 160 solution points. The numbers of solution points in the x-, y- and z-directions are 2580, 444 and 258, respectively. As shown in part I, the resolution of the current grid is high enough to calculate all relevant turbulent scales and energy budget terms accurately.

2.5. *Initial conditions*

In this work, we use the inlet boundary layer thicknesses reported by Monkewitz & Heurre (1982). The inflow conditions are carefully set to be nearly identical for all three cases. The two laminar boundary layers, specified to a 99 % thickness ratio, $\lambda = \delta_2/\delta_1 = 1.6$ at the inflow section of the computational domain, evolve along both sides of the splitter plate (Monkewitz & Heurre 1982; McMullan, Gao & Coats 2009). The subscripts 1 and 2 indicate the high- and low-speed sides, respectively. The two fully developed Blasius boundary layers traverse the trailing edge of the splitter plate and merge into an FSL

downstream (Li *et al.* 2019). The configuration of the splitter plate is illustrated in figure 1 (for the detailed description of the FSL initial conditions, readers are referred to Li *et al.* (2019)).

Note that Laizet & Lamballais (2006) observed unrealistic flow dynamics when they employed two laminar streams to initialize a mixing layer without any inflow perturbations. The authors later concluded that the unrealistic results are due to the lack of 3-D instabilities downstream of the trailing edge (Laizet, Lardeau & Lamballais 2010). Based on the insights from the previous studies (Laizet & Lamballais 2006; Laizet *et al.* 2010), we conducted extensive tests to obtain the optimal level of instabilities. Consequently, a small perturbation is superimposed on the upper boundary layer (Li *et al.* 2019). This perturbation allows a realistic initial development of disturbances, ensuring a naturally developing destabilization in the boundary layer at the trailing edge of the splitter (Laizet *et al.* 2010). A stochastic model proposed by Gao & Mashayek (2004) is utilized to generate perturbations. The stream in the low-speed side is laminar and lacks perturbations (Sandham & Sandberg 2009). Note that no forcing mechanism is applied in either inflow boundary layers (Sandham & Sandberg 2009; Laizet *et al.* 2010; Sharma, Bhaskaran & Lele 2011; Pirozzoli *et al.* 2015).

The Reynolds numbers of the two inlet boundary layers are $Re_{\theta 1} = 200$ (based on U_1 and $\delta_{\theta 1}$) and $Re_{\theta 2} = 60$ (based on U_2 and $\delta_{\theta 2}$), respectively (Li *et al.* 2019). Here, $\delta_{\theta 2}$ is the initial momentum thickness of the lower boundary layer (low-speed side), and is evaluated just upstream of the trailing edge. With the artificially generated perturbation (Laizet *et al.* 2010), both these Reynolds numbers are not sufficiently large for a laminar boundary layer to develop any turbulence. The dimensionless temperature and density are uniformly initialized to $(\Delta U/2M_c)^2$ and 1.0, respectively. The length of the splitter plate is sufficiently long ($L_s = 182$), so that the fully developed Blasius profiles at the end of the splitter plate are nearly identical to the boundary layer inlet conditions used by Monkewitz & Heurre (1982). Note that when the flow reaches self-similarity, the trace of the initial conditions has been completely purged (Bradshaw 1966).

To obtain the necessary statistics, all cases undergo the following processes. Each simulation is initially run for 64 000 time steps to purge the transient flow and reach a quasi-stationary state. Another 64 000 time steps are used to compute the first-order statistics. Next, 128 000 time steps are required to obtain sufficient information for the second-order statistics. Finally, we implement post-processing for ensemble averages in the spanwise direction to enhance the accuracy of the statistics. All simulations are performed using 2048 cores on AMD Opteron 6276 Interlagos (Bode *et al.* 2013; Kramer *et al.* 2015). The computational time steps are fixed at $\Delta t = 0.0446, 0.0268, 0.0192$ for the cases with $M_c = 0.3, 0.5, 0.7$, respectively.

3. Energy exchange

Following the work of Huang *et al.* (1995), the TKE, MKE and MIE transport equations for a stationary flow are, respectively, expressed as

$$\frac{\partial \langle \rho \rangle \{u_k\} \{k\}}{\partial x_k} = \underbrace{-\langle \rho \rangle \{u_i'' u_k''\} \frac{\partial \{u_i\}}{\partial x_k}}_{\mathcal{P}} - \frac{\partial \langle \rho \rangle \{u_k'' k''\}}{\partial x_k} - \frac{\partial \langle p' u_k' \rangle}{\partial x_k}$$

$$+ \frac{\partial \langle \tau_{ik}' u_i' \rangle}{\partial x_k} - \underbrace{\left\langle \tau_{ik}' \frac{\partial u_i'}{\partial x_k} \right\rangle}_{\varepsilon} - \underbrace{\langle u_k'' \rangle \frac{\partial \langle p \rangle}{\partial x_k}}_{\Psi} + \langle u_i'' \rangle \frac{\partial \langle \tau_{ik} \rangle}{\partial x_k} + \underbrace{\left\langle p' \frac{\partial u_k'}{\partial x_k} \right\rangle}_{\Pi}, \qquad (3.1)$$

$$\frac{\partial \langle \rho \rangle \{u_k\} \{K\}}{\partial x_k} = \underbrace{\langle \rho \rangle \{u_i'' u_k''\} \frac{\partial \{u_i\}}{\partial x_k}}_{-\mathcal{P}} - \frac{\partial \langle \rho \rangle \{u_k'' K''\}}{\partial x_k} - \frac{\partial \langle p \rangle \langle u_k \rangle}{\partial x_k} + \frac{\partial \langle \tau_{ik} \rangle \langle u_i \rangle}{\partial x_k}$$

$$- \underbrace{\langle \tau_{ik} \rangle \frac{\partial \langle u_i \rangle}{\partial x_k}}_{\varPhi} + \langle p \rangle \frac{\partial \langle u_k \rangle}{\partial x_k} + \underbrace{\langle u_k'' \rangle \frac{\partial \langle p \rangle}{\partial x_k}}_{\varPsi} - \langle u_i'' \rangle \frac{\partial \langle \tau_{ik} \rangle}{\partial x_k} \tag{3.2}$$

and

$$\frac{\partial \langle \rho \rangle \{u_k\} \{e\}}{\partial x_k} = \underbrace{\langle \tau_{ik} \rangle \frac{\partial \langle u_i \rangle}{\partial x_k}}_{\varPhi} + \underbrace{\left\langle \tau_{ik}' \frac{\partial u_i'}{\partial x_k} \right\rangle}_{\varepsilon} - \frac{\partial \langle \rho \rangle c_v \{u_k'' T''\}}{\partial x_k}$$

$$- \frac{\partial \langle q_k \rangle}{\partial x_k} - \langle p \rangle \frac{\partial \langle u_k \rangle}{\partial x_k} - \underbrace{\left\langle p' \frac{\partial u_k'}{\partial x_k} \right\rangle}_{\varPi}. \tag{3.3}$$

The molecular mean stress and fluctuating stress are, respectively,

$$\langle \tau_{ik} \rangle = \left[\mu \left(\frac{\partial \langle u_i \rangle}{\partial x_k} + \frac{\partial \langle u_k \rangle}{\partial x_i} \right) - \frac{2}{3} \mu \frac{\partial \langle u_l \rangle}{\partial x_l} \delta_{ik} \right] \tag{3.4}$$

and

$$\tau_{ik}' = \left[\mu \left(\frac{\partial u_i'}{\partial x_k} + \frac{\partial u_k'}{\partial x_i} \right) - \frac{2}{3} \mu \frac{\partial u_l'}{\partial x_l} \delta_{ik} \right], \tag{3.5}$$

with the assumption that the dynamic viscosity of the fluid is independent of temperature (see § 2.1).

Based on the common literature (Favre 1965, 1969; Lele 1994; Huang *et al.* 1995; Pope 2000), the term on the left-hand side (LHS) of (3.1) represents kinetic energy convection. The first term on the right-hand side (RHS) is the turbulent production; the second, turbulent convection; the third, pressure transport; the fourth, viscous diffusion; the fifth, turbulent viscous dissipation; the sixth, enthalpic production; the seventh, a compressibility term resulting from turbulent fluctuations; the last, a pressure-dilatation correlation. The last three terms on the RHS of (3.1) are compressibility related terms due to turbulent fluctuations. Terms one $(-\langle \rho \rangle \{u_i'' u_k''\} \partial \{u_i\}/\partial x_k)$, six $(\langle u_k'' \rangle \partial \langle p \rangle/\partial x_k)$ and seven $(\langle u_i'' \rangle \langle \tau_{ik} \rangle/x_k)$ on the RHS of (3.1) are also in (3.2) but with an opposite sign. They are responsible for the energy exchange between the mean and turbulent kinetic energies. Terms five $(\langle \tau_{ik}'(\partial u_i'/\partial x_k) \rangle)$ and eight $(\langle p'(\partial u_k'/\partial x_k) \rangle)$ in (3.1) correspond to terms two and six in (3.3), which account for the energy exchange between the internal and turbulent kinetic energies. Besides the common terms in (3.1) and (3.2), the term on the LHS of (3.2) is MKE convection. The second term on the RHS of (3.2) is mean turbulent convection; the third, mean pressure transport due to mean velocity–pressure interaction; the fourth, mean viscous diffusion; the fifth, mean energy dissipation; and the sixth, mean pressure dilatation. The mean energy dissipation and mean pressure dilatation of (3.2) also appear in (3.3) with an opposite sign. These two terms account for the energy exchange between internal and mean kinetic energies. For the rest of the terms in (3.3), the third and fourth terms on the RHS are internal energy diffusion and heat conduction, respectively; the term on the LHS represents MIE convection (Favre 1969; Lele 1994; Huang *et al.* 1995).
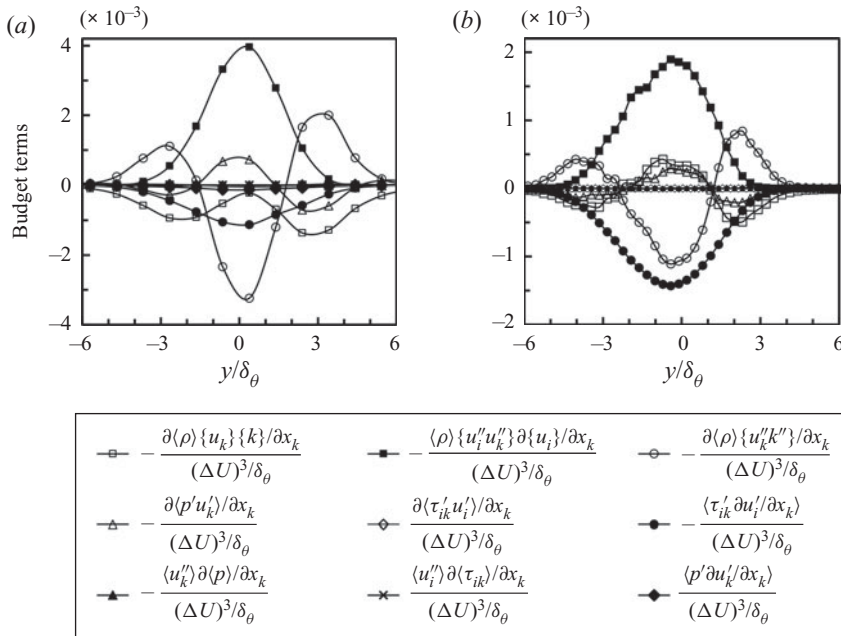
FIGURE 3. Cross-stream profiles of all the budget terms in (3.1) for $M_c = 0.3$ at (a) $x - x_R = 200$ and (b) $x - x_E = 500$. All terms are normalized by $(\Delta U)^3/\delta_\theta$.

Turbulent energy exchange can be accomplished through energy redistribution in space and energy conversion among different forms of energy (budget terms in TKE, MKE and MIE transport equations). Turbulent transport budget terms account for convection and diffusion of TKE and play significant roles in spatial energy redistribution. These terms have nearly the same order of magnitude as turbulent production and dissipation, and therefore balance the budget equations. One such example is shown in figure 3 for (3.1). Figure 3 reveals the cross-stream profiles of all the budget terms in (3.1) for $M_c = 0.3$ at two streamwise locations, $x - x_R = 200$ and $x - x_E = 500$. All the budget terms are normalized by $(\Delta U)^3/\delta_\theta$. As expected, the kinetic energy convection, $-\partial\langle\rho\rangle\{u_k\}\{k\}/\partial x_k$, the turbulent convection, $-\partial\langle\rho\rangle\{u_k''k''\}/\partial x_k$ and the pressure transport, $-\partial\langle p'u_k'\rangle/\partial x_k$, have significant energy contributions along the cross-stream direction, and mainly balance the turbulent energy at the edge of the FSL, where the production goes to zero. However, in this work, we focus on the kinetic energy conversion among various forms of energy in the three kinetic energy transport equations, rather than the kinetic energy redistribution in space.

Based on our DNS results of all the budget terms in the three transport equations, five terms are found to be mainly responsible for the turbulent energy conversion among TKE, MKE and MIE: turbulent production, $\mathcal{P} = -\langle\rho\rangle\{u_i''u_k''\}\partial\{u_i\}/\partial x_k$; turbulent viscous dissipation, $\varepsilon = \langle\tau_{ik}'(\partial u_i'/\partial x_k)\rangle$; mean viscous dissipation, $\Phi = \langle\tau_{ik}\rangle\partial\langle u_i\rangle/\partial x_k$; turbulent pressure dilatation, $\Pi = \langle p'(\partial u_k'/\partial x_k)\rangle$; and enthalpic production, $\Psi = \langle u_k''\rangle\partial\langle p\rangle/\partial x_k$. Figure 4 shows the simplified schematic of the kinetic energy transfer corresponding to the current DNS results (for the detailed schematic of kinetic energy balance, readers are referred to Lele (1994) and Mittal & Girimaji (2019)). In the figure, we only present the dominant terms responsible for energy exchange among TKE, MKE and MIE. The directions of energy exchange are also illustrated in the figure corresponding to the positive
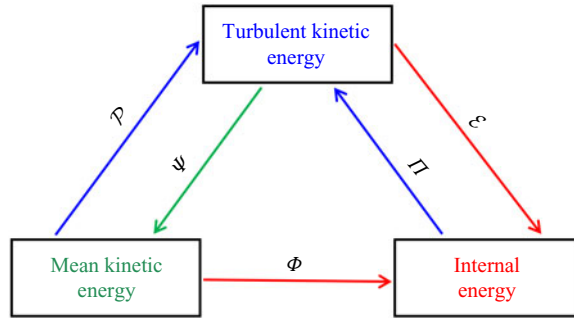
FIGURE 4. Direction of energy exchange among TKE, MKE and MIE, assuming the budget term is positive in the FSL flow study in this work.

values of budget terms in the FSL flow. For instance, if the value of $\mathcal{P}$ is positive, then following the corresponding arrow in figure 4, the direction of energy transfer is from MKE to TKE.

Turbulent and enthalpic production transfer energy between the mean and turbulent kinetic energies. The turbulent production is the product of Reynolds stresses and the gradients of mean velocity components. This budget term is mainly responsible for transferring kinetic energy from the mean shear flow to the turbulent fluctuating shear flow. When $\mathcal{P}$ is positive, the energy is converted from MKE (mainly large-scale structures) to TKE (primarily small-scale structures), and vice versa. Therefore, this term represents no net loss or gain of kinetic energy but a transfer between mean and turbulent components. The enthalpic production term, Ψ, produces enthalpic energy and causes a gain or loss of TKE. Here Ψ can have either sign; a negative value represents a loss from MKE and gain of TKE. This energy conversion alters the mean entropy and thus is regarded as irreversible. The mean entropy, Υ, is defined as (Favre 1969; Lele 1994)

$$\Upsilon = \frac{\partial \langle \rho \rangle \langle s \rangle \langle u_k \rangle}{\partial x_k} + \frac{\partial \langle \rho \rangle \{s'' u_k''\}}{\partial x_k} + \frac{\partial \langle q_k/T \rangle}{\partial x_k}, \tag{3.6}$$

where s is specific entropy.

The turbulent viscous dissipation and pressure-dilatation terms convert energy between TKE and MIE. Here ε is mainly responsible for the energy exchange from turbulent kinetic to internal energies through molecular viscosity. On the other hand, Π is the net rate of work done by pressure fluctuations due to the simultaneous fluctuations in dilatation (Lele 1994). Here Π may manifest either sign, and when negative, it represents a loss from TKE and gain of MIE. This energy exchange does not change the mean entropy and thus can be regarded as reversible. In regions with negligible mean acceleration and insignificant mean volume change, Π can also be interpreted as an exchange with acoustic potential energy (Lele 1994). The mean viscous dissipation, Φ, transfers energy between internal and mean kinetic energies. Here Φ is the dissipation due to the mean flow and transfers the MKE to MIE through molecular viscosity.

The growth of the plane FSL primarily consists of two stages: the laminar–turbulent transition stage (the rapidly evolving stage) and the self-similar turbulent stage (the steady growing stage). In the first stage, the fundamental mode of instability, Kelvin–Helmholtz instability, begins to develop, and the vortex starts to roll up (Rogers & Moser 1992). Then, the adjacent vortices begin to pair and the 2-D primary spanwise coherent structures become dominant. In the braid region of the 2-D spanwise coherent structures, the 3-D

secondary streamwise vortex structures appear and stretch the 2-D primary spanwise structures to break them down to small-scale vortex structures (Olsen & Dutton 2003). The interaction between the 2-D primary and 3-D secondary instabilities promotes the transition from laminar to turbulent flow, leading to a self-similar state (Pierrehumbert & Widnall 1982; Hussaini & Voigt 1990; Sandham & Reynolds 1991). In the second stage, the self-similarity is achieved, and the flow has forgotten the inflow conditions (Bradshaw 1966). Due to the large difference in the behaviours of the two stages, we separately investigate the compressibility effect on the energy exchange in the transition and turbulent regions. Based on our previous work, part I, the locations (x_R), where the turbulence transition starts, are approximated as 30, 170 and 230, while the locations (x_E), where the turbulent transition completes are estimated as 340, 550 and 670, for $M_c = 0.3$, 0.5 and 0.7, respectively (see table 1). The remainder of this section is structured as follows. First we discuss the energy exchange among TKE, MKE and MIE in the transition region, then in the turbulent region. Finally, the components of the turbulent production and viscous dissipation, as well as the energy exchange are examined.

3.1. *Laminar–turbulent transition region*

We study the energy exchange among TKE, MKE and MIE, and the compressibility effect on them in the transition region via both qualitative and quantitative analyses. Figures 5–7 show the contours of $\mathcal{P}$, ε, Φ, Π and Ψ for $M_c = 0.3$, 0.5 and 0.7, respectively, with a break at $x = x_E$ separating the transition and turbulent regions. Since the initial velocity field is laminar (see part I for more detail), the normalized values of $\mathcal{P}$, ε, Π and Ψ are relatively small at the beginning of the shear layer. In contrast, Φ starts with a large value due to the considerable mean shear of two mean streams at the trailing edge of the splitter. As the shear layer develops, the flow instability increases; the turbulent production significantly outweighs the turbulent viscous dissipation, such that the kinetic energy grows. The extrema of $\mathcal{P}$, ε, Π and Ψ shift to downstream, except Φ, which remains somewhat insensitive to the variation of the convective Mach number.

The cross-stream profiles of $\mathcal{P}$, ε, Φ, Π and Ψ are considered for the examination of the energy exchange and the compressibility effect on energy exchange. Figure 8 compares the normalized cross-stream profiles of the aforementioned five terms for $M_c = 0.3$, 0.5 and 0.7, respectively, at $x - x_R = 200$ near the middle of the laminar–turbulent region. Two peaks can be observed for Ψ over the cross-stream direction. One peak appears near the centre of the low-speed side of the shear layer, while another is approximately in the middle of the high-speed side. The centre of the shear layer becomes a valley and has the lowest value. These might be because the mean pressure gradients with respect to the cross-stream direction are larger at the edges of the high- and low-speed sides of the shear layer, and the magnitudes of $\langle v'' \rangle$ are higher as well, compared with the centre of the shear layer. However, the mean pressure gradient with respect to the streamwise direction is insignificant, due to the nature of the compressible FSL flow, i.e. zero pressure gradient with respect to the flow direction. When the mean pressure gradient with respect to the cross-stream direction acts on the flow, the work done by the mean pressure gradient becomes a gain in the kinetic energy, resulting in two peaks along the cross-stream direction. The compressibility effect on the cross-stream variations of five budget terms is also demonstrated in figure 8. The peaks of the normalized $\mathcal{P}$, ε and Π decrease with increasing M_c, indicating that in the transition region, the normalized energy that transfers through $\mathcal{P}$, ε and Π decreases with increasing compressibility. However, the magnitudes of the normalized Φ for all cases remain nearly constant with the change of M_c,
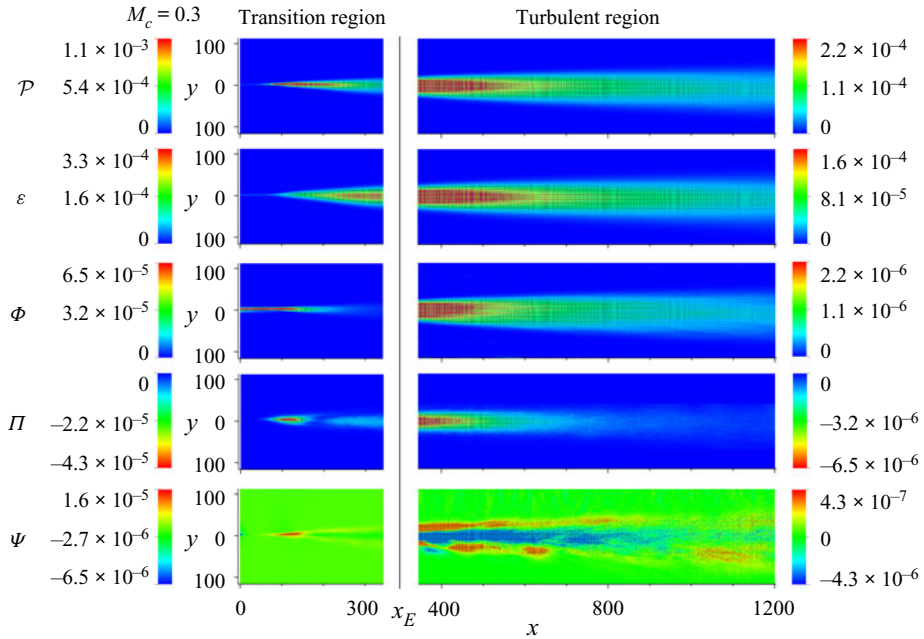
FIGURE 5. Contours of $\mathcal{P}$, ε, Φ, Π and Ψ for $M_c = 0.3$ in the transition and turbulent regions separated by a vertical line at $x = x_E$. All terms are normalized by $(\Delta U)^3$.

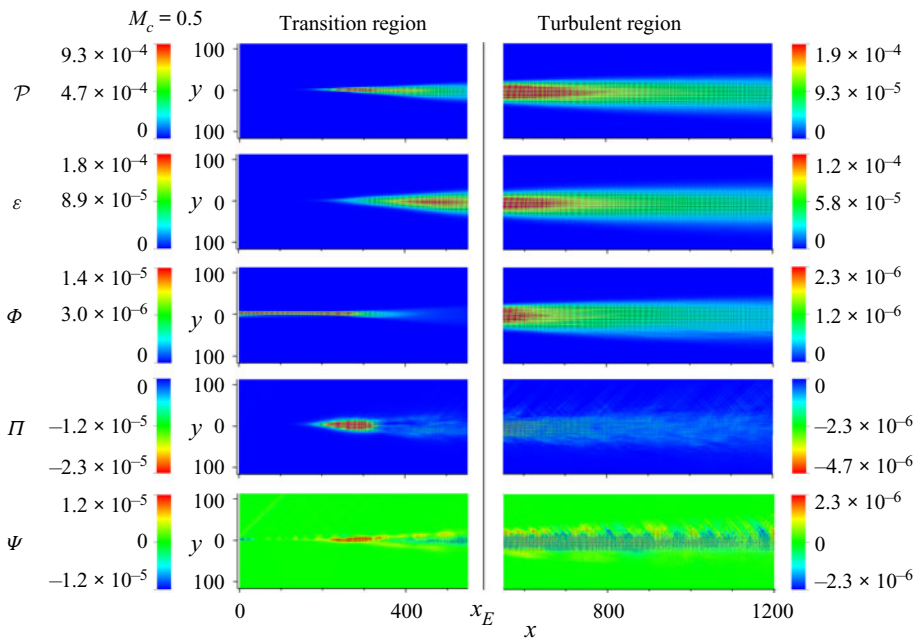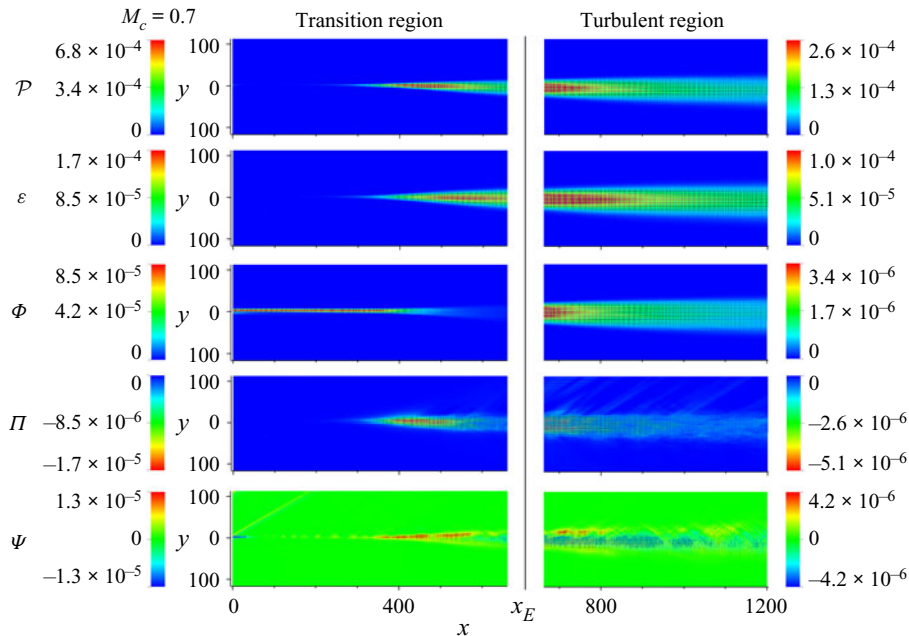FIGURE 6. Contours of $\mathcal{P}$, ε, Φ, Π and Ψ for $M_c = 0.5$ in the transition and turbulent regions separated by a vertical line at $x = x_E$. All terms are normalized by $(\Delta U)^3$.

FIGURE 7. Contours of $\mathcal{P}$, ε, Φ, Π and Ψ for $M_c = 0.7$ in the transition and turbulent regions separated by a vertical line at $x = x_E$. All terms are normalized by $(\Delta U)^3$.

suggesting that the normalized energy exchange through Φ is almost unaffected by compressibility. With increasing M_c, the value of the normalized Ψ at the centre of the shear layer is unchanged, while the magnitudes of the two adjacent peaks increase, implying that the energy transferred through Ψ from TKE to MKE increases at the two sides of the shear layer.

Figure 9(a) compares the magnitudes of the normalized $\mathcal{P}$, ε, Φ, Π and Ψ, at the lower edge ($y = -18.63$), centre ($y = y_{0.5}$) and upper edge ($y = 17.53$) along the cross-stream direction of the shear layer at $x_R = 200$ for $M_c = 0.3$. Here, $y_{0.5}$ is the lateral position at which the streamwise velocity reaches the convective velocity, U_c, in the cross-stream direction, where U_c is defined as

$$U_c = \frac{U_1 + U_2}{2}. \tag{3.7}$$

At the lower and upper edges of the shear layer, the magnitudes of all five terms are insignificant, while at the shear layer centre, the turbulent production and turbulent viscous dissipation terms have significant contributions to the energy exchange. Note that the ratio of $\mathcal{P}$ to ε at the centre of the shear layer is approximately 3.5, meaning that in the transition region, the turbulent production considerably outweighs the turbulent viscous dissipation; hence the kinetic energy significantly grows. Figure 9(b) compares the magnitudes of the normalized $\mathcal{P}$, ε, Φ, Π and Ψ, for various M_c at the centre of the shear layer. It is clearly shown that both the normalized $\mathcal{P}$ and ε are significantly affected by compressibility; the normalized $\mathcal{P}$ and ε decrease as M_c increases. However, other terms appear nearly unchanged with various M_c, because of the adopted scale in the figure and their smaller contributions to the kinetic energy exchange, compared with that of $\mathcal{P}$ and ε.
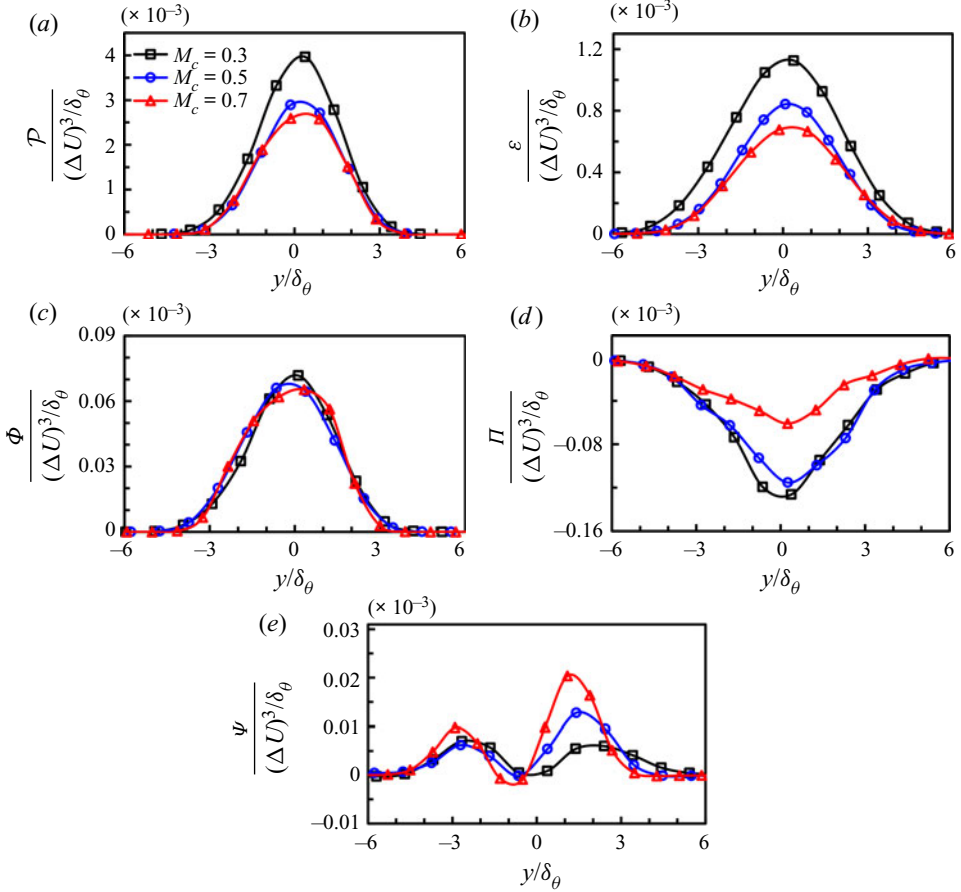
FIGURE 8. Cross-stream variation of (*a*) $\mathcal{P}$, (*b*) ε, (*c*) Φ, (*d*) Π and (*e*) Ψ for $M_c = 0.3, 0.5,$ 0.7. All terms are extracted at $x - x_R = 200$ in transition region and normalized by $(\Delta U)^3/\delta_\theta$.
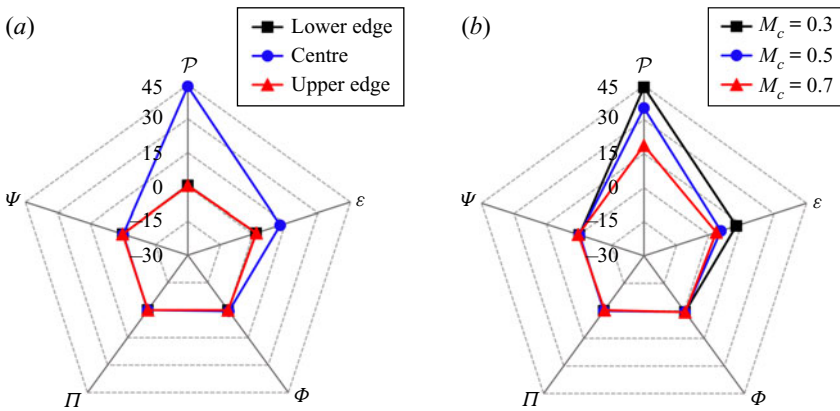

FIGURE 9. Comparisons of $\mathcal{P}$, ε, Φ, Π and Ψ, (*a*) at the lower edge ($y = -18.63$), centre ($y = y_{0.5}$) and upper edge ($y = 17.53$) of the shear layer for $M_c = 0.3$, (*b*) at the centre of the shear layer for $M_c = 0.3, 0.5$ and 0.7, in transition region at $x - x_R = 200$. All terms are normalized by $(\Delta U)^3/\delta_\theta \times 10^{-4}$.

The influence of compressibility on energy exchange is further investigated by considering the evolution of the cross-stream integral, ϕ^I, which is defined as

$$\phi^I = \int_{-\infty}^{+\infty} \phi \, \mathrm{d}y. \tag{3.8}$$

Here, ϕ represents any budget term that transfers energy among TKE, MKE and MIE. The superscript I represents the cross-stream (y-line) integration. Since the aforementioned budget terms evolve in the streamwise direction and expand in the cross-stream direction, their cross-stream integral can provide information about their bulk behaviour and help to understand their energy exchange contributions along the streamwise direction.

Figure 10 presents the normalized $\mathcal{P}^I$, ε^I, Φ^I, Π^I and Ψ^I as a function of $x - x_R$ in the transition region, for various M_c. As a result, we can compare the evolution of these budget terms for different Mach numbers with the same start locations of the turbulent transition region. Note that this streamwise evolution can only be observed in the spatially developing FSL but not in the temporally developing numerical simulations. The terms $\mathcal{P}^I$, ε^I, Π^I and Ψ^I start with a nearly zero magnitude, until perturbations grow, and their magnitudes increase. In contrast, Φ^I initiates with an extremum followed by a slow decline towards an asymptotic value. This means that the energy exchange from MKE to other forms of energy through Φ^I mainly occurs at the beginning of the shear flow. The evolutions of budget terms for different cases are significantly affected by the change of M_c, as observed in figure 10. The influence of compressibility for the normalized $\mathcal{P}^I$, ε^I, Π^I and Ψ^I becomes more significant as the flow advances downstream, but the normalized Φ^I remains nearly unchanged. The peaks of the normalized $\mathcal{P}^I$, ε^I and Π^I decrease as M_c increases, while the peak of the normalized Ψ^I increases. We can conclude that, in the transition region with increasing compressibility, the energy that transfers through $\mathcal{P}$, ε and Π decreases; energy exchange through Φ is nearly unchanged; energy exchange through Ψ increases.

We can observe a double-peak variation of $\mathcal{P}^I$ for $M_c = 0.3$ and 0.5 in figure 10(a). This phenomenon can be explained with the flow vortex structures. To inspect further, we present the corresponding enlarged area in figure 11(a). It can be seen that the magnitude of turbulent production rapidly rises at the position near the trailing edge, where the large structures dominate the flow. The value at the first peak ($x \approx 130$) is roughly 2.6 times that at $x \approx 1000$ in the self-similar region, while the second peak value is roughly 94 % of the first peak value. Note that the double peak spans from $x \approx 130$ to 240, which is within the transition area. To the best of our knowledge, this double-peak phenomenon has not been reported in the literature for planar free shear flows. We propose that two significant vortex pairings cause this kind of phenomenon.

We can relate the double-peak profile directly to the rise of the pairing vortex, based on the visualization of the flow structures presented in figure 11(b). Careful observation shows that the positions of the peaks, at $x \approx 130$ and 240, are in the same streamwise areas where the pairings occur, illustrated in the vorticity contours. This observation hints at the connection between the double peak and the behaviour of the vortex pairings. We further examine the evolution of the 3-D structures in the flow to understand how the vortex pairing leads to a peak of turbulent production. Figure 11(c) presents a 3-D representation of the turbulent structures via the isosurface of the second invariant of the velocity gradient tensor. From figure 11(c), the newly generated 2-D primary spanwise coherent structures near the trailing edge of the splitter form the first pairing at roughly $x = 130$. The first pairing generates a large vortex structure (which does not break into small vortices)
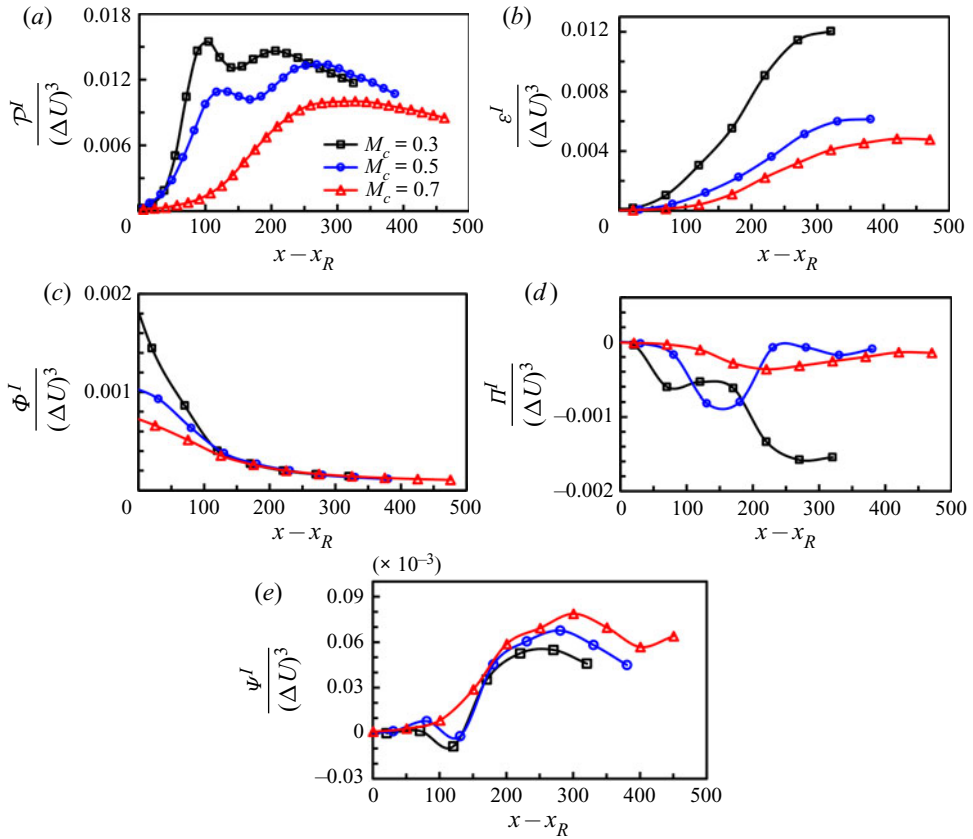
FIGURE 10. Evolution of the cross-stream integrals (*a*) $\mathcal{P}^I$, (*b*) ε^I, (*c*) Φ^I, (*d*) Π^I and (*e*) Ψ^I for $M_c = 0.3$, 0.5 and 0.7 in the transition region. All terms are normalized by $(\Delta U)^3$.
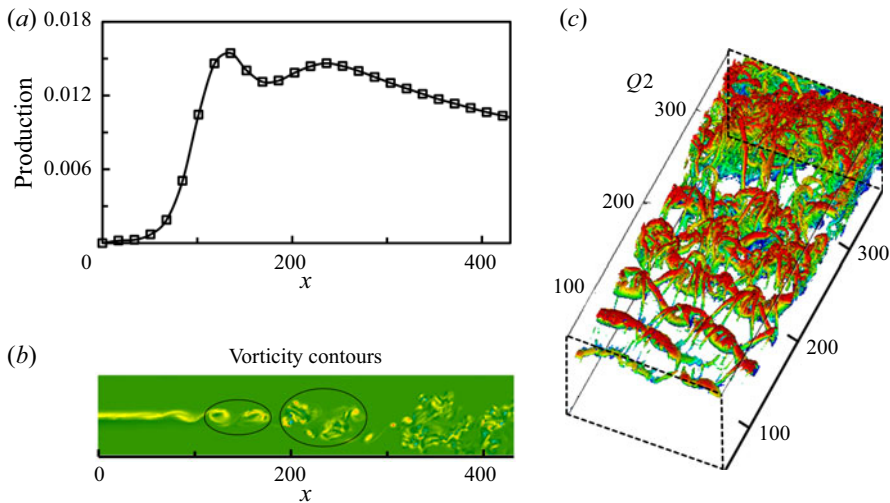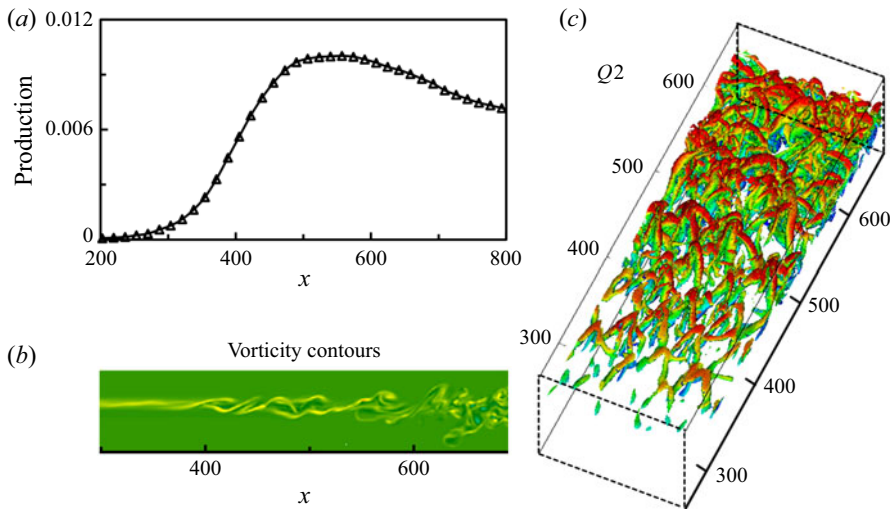

FIGURE 11. (*a*) Evolution of $\mathcal{P}^I$ normalized by $(\Delta U)^3$, (*b*) spanwise vorticity contours and (*c*) isosurface of the second invariant of the velocity gradient tensor ($Q2 = 0.02$), coloured by streamwise velocity, for $M_c = 0.3$ in transition region.

FIGURE 12. (*a*) Evolution of $\mathcal{P}^I$ normalized by $(\Delta U)^3$, (*b*) spanwise vorticity contours and (*c*) isosurface of the second invariant of the velocity gradient tensor ($Q2 = 0.02$), coloured by streamwise velocity, for $M_c = 0.7$ in transition region.

(Ho & Huang 1982; Moser & Rogers 1993). A large paired vortex structure maintains more kinetic energy than an unpaired roller vortex structure, and less dissipation than a paired vortex with broken-down structures (Sandham 1989). Therefore, the first peak of turbulent production occurs due to the appearance of the first pairing.

The large vortex structure formed by the first pairing continues rotating, twisting and stretching. As the intensity of the instability grows and reaches a triggering threshold level, the second pairing occurs and leads to the second peak of the turbulent production (Sandham 1989). At the same time, large vortex structures swirl into flower-shaped vortices, which start to play a dominant role in the breakdown of the mixing layer. The slender petals of the flower-shaped vortices develop with intense vorticity and break down into small vortices. These small vortices facilitate more dissipation and preserve less kinetic energy, making the second peak of turbulent production lower than the first peak. Subsequently, the flower-shaped vortices then evolve into hairpin vortices downstream, and more and more small vortices are generated near the centre of the hairpin vortices. The turbulent production gradually decreases as the flow advances downstream because the rate of turbulent viscous dissipation increases as the number of small vortices increases.

For the $M_c = 0.7$ case, only one peak appears in the profile of turbulent production, shown in figure 12(*a*). The single peak is because the 3-D secondary streamwise vortex structures become dominant in the roll-up region of the shear layer, which is demonstrated in figure 12(*c*) as well. The streamwise vortex structures then develop into lambda-shaped vortices (Sandham & Reynolds 1990, 1991; Lui & Lele 2001; Fu & Li 2006; Zhou, He & Shen 2012; Zhang, Tan & Yao 2019), which are subjected to longitudinal elongation due to the high compressibility. These elongated vortex structures have less tendency to roll or pair in the streamwise direction (see figure 12*b*). The unpaired vortex structures directly evolve into hairpin vortices without experiencing rolling. The kinetic energy grows as the flow advances downstream. Prior to the point that the turbulent viscous dissipation becomes significant, the magnitude of turbulent production peaks. Next, small vortices dominate the flow, leading to a smooth decay of turbulent production.
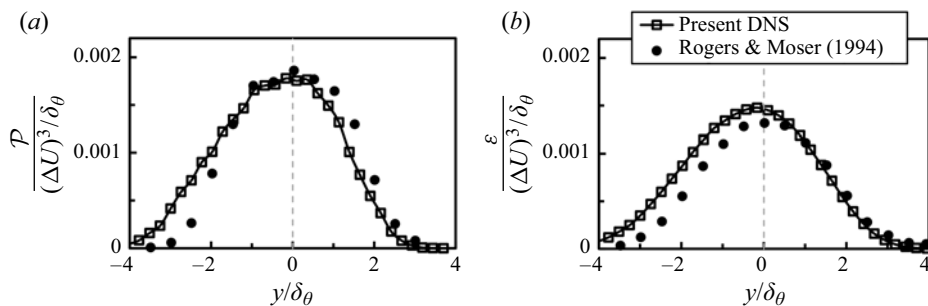
FIGURE 13. Comparison of cross-stream profiles from the present work and the results by Rogers & Moser (1994) for (*a*) turbulent production and (*b*) turbulent viscous dissipation at $x - x_E = 300$ in the self-similar turbulent region for $M_c = 0.3$. All terms are normalized by $(\Delta U)^3/\delta_\theta$.

3.2. *Self-similar turbulence region*

In this section, we investigate the evolutions of $\mathcal{P}$, ε, Φ, Π and Ψ, as well as the compressibility effects on them in the self-similar turbulent region. We compare the evolutions of the budget terms for different M_c using a shifted streamwise axis, $x - x_E$. Consequently, we are able to examine the behaviours of the budget terms by eliminating the effect from the unequal laminar–turbulent transition lengths. Contours of the normalized $\mathcal{P}$, ε, Φ, Π and Ψ for all cases are presented in figures 5–7. We can see that the start of the turbulent region significantly shifts to downstream with increasing M_c (see part I for more details). As the flow advances downstream, $\mathcal{P}$, ε, Φ, Π and Ψ decrease gradually, while expanding in the cross-stream direction, especially for $\mathcal{P}$, ε and Φ, which grow linearly. This is attributed to the self-similarity nature of the FSL flow in the turbulent region.

In figures 13(*a*) and 13(*b*), we compare the cross-stream profiles of the normalized turbulent production and turbulent viscous dissipation from present simulations with the results by Rogers & Moser (1994), generated from the DNS of a temporally evolving shear layer. Both results are extracted from the self-similar turbulent region for $M_c = 0.3$. The profiles from the present work noticeably shift to the low-speed side ($y < 0$) of the shear layer, compared with the result of Rogers & Moser (1994). Despite the profiles shifting, the normalized values of turbulent production and dissipation are in agreement, confirming that the turbulent shear layer is correctly resolved. Note that the shear-layer bending is only captured in the spatially evolving turbulent shear layer simulations. We discuss the shear-layer bending in detail next.

To further investigate the shear-layer bending phenomenon, we start from the velocity isolines at the centre (U_c), upper-edge ($95 \% U_1$) and lower-edge ($105 \% U_2$) of the shear layer along the streamwise direction. As a result, the outline of the shear layer in the $x-y$ plane can be inspected. Figure 14(*a*) shows the velocity isolines of $95 \% U_1$, U_c and $105 \% U_2$ for various M_c. We can see that as the convective Mach number increases, the growth rate of the shear layer decreases, resulting in a narrower shear layer contour. Moreover, the momentum thickness growth rates, $\mathrm{d}\delta_\theta/\mathrm{d}x$, in the turbulent region are computed as 0.0137, 0.0121 and 0.0106 for convective Mach numbers of 0.3, 0.5 and 0.7, respectively (see table 2). This trend confirms that the momentum thickness growth rate decreases as M_c increases (Birch & Eggers 1972; Papamoschou & Roshko 1988; Jackson & Grosch 1989; Goebel & Dutton 1991; Grosch & Jackson 1991; Hall, Dimotakis & Rosemann 1993; Clemens & Mungal 1995; Vreman, Sandham & Luo 1996;
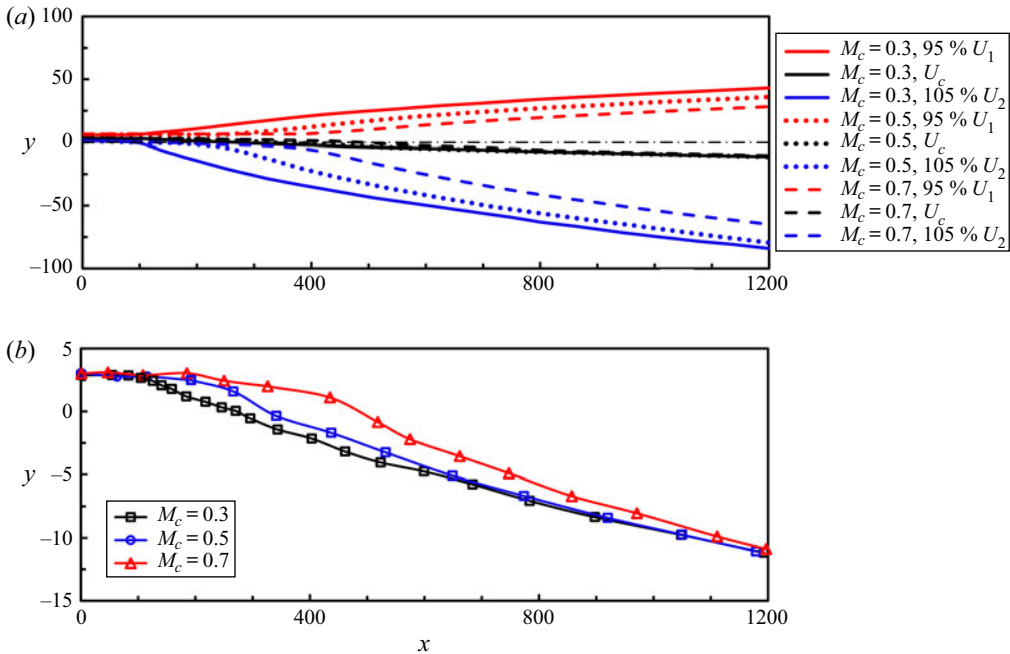
FIGURE 14. (*a*) Mean velocity isolines and (*b*) isolines of U_c for various M_c, as a function of x.

Day, Reynolds & Mansour 1998; Freund, Lele & Moin 2000; Pantano & Sarkar 2002; Foysi & Sarkar 2010; Javed, Rajan & Chakraborty 2013; Wang *et al.* 2015). In figure 14(*a*), the U_c contours are qualitatively similar for any given M_c, although there are some small differences in the contours in the transition region of the shear layer.

A closer look at the U_c contours helps to identify the compressibility effect on shear-layer bending, as shown in figure 14(*b*). The shift to the low-speed side starts from $x \approx x_R$. For a more explicit comparison, we normalize the streamwise axis as $x - x_R$ and add trendlines to all cases, shown in figure 15. The figure reveals that the centre of the shear layer extends further into the low-speed side as the convective Mach number increases (see figure 15*b*). This finding may help to explain the phenomenon in the backward-facing step (known as BFS) flow, where the reattachment length decreases as the inflow Mach number increases (Chen *et al.* 2012; Liu *et al.* 2013). This shifting of the mean velocity profile in the FSL has been reported in previous studies, both experimental and numerical (Elliott & Samimy 1990; Goebel & Dutton 1991; Fu & Li 2006). However, a detailed explanation of such behaviour is not available. In this work, we explain this behaviour quantitatively in terms of the asymmetry mass flux entrainment of the shear layer.

In a plane FSL with different free stream speeds, the flow field can be classified into two regions: in one region the flow is primarily irrotational; in the another one the flow is mainly turbulent and rotational. Entrainment is the process that the mass flux traverses from the irrotational region into the rotational area (Corrsin & Kistler 1955). The mass flux entrainment ratio (R_M) is defined as the ratio of the fluid from the high-speed side to the fluid from the low-speed side into the shear layer. The mass flux entrainment ratio for an incompressible, plane FSL can be estimated by (Dimotakis 1986)

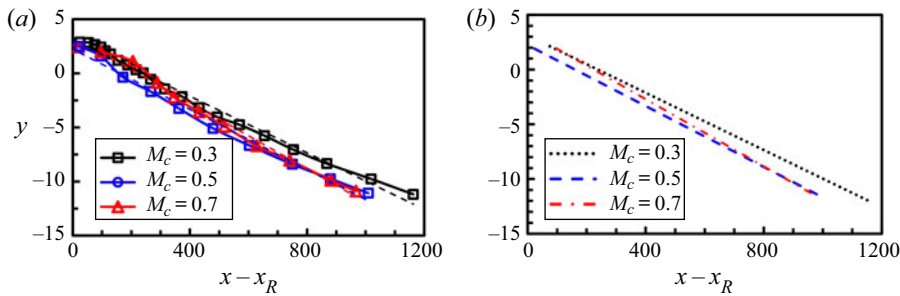$$R_M = 1 + 3.9 \frac{\delta_w}{x}, \tag{3.9}$$

FIGURE 15. (*a*) Isolines of U_c and (*b*) trendlines of the isolines for $M_c = 0.3$, 0.5 and 0.7, as a function of $x - x_R$.

where $\delta_w = \Delta U / (\mathrm{d}\{u\}/\mathrm{d}y)_{max}$ is the vorticity thickness. The empirical constant 3.9 was suggested by Koochesfahani *et al.* (1979). Dimotakis (1986) also proposed a simplified equation to determine the mass flux entrainment ratio in the turbulent region of the shear layer, i.e.

$$R_M = 1 + 0.68R, \tag{3.10}$$

where R is the velocity ratio defined by (2.13). The results calculated by (3.9) and (3.10) are plotted in figure 16(*a*) as a function of x for $M_c = 0.3$. We can see that the result estimated by (3.9) starts with a relatively low value of 1.2 at $x \approx 100$. As advancing downstream, the magnitude gradually increases and overtakes the result calculated by (3.10) at $x \approx 200$ in the transition region. It means that the entrainment ratio in the transition region is slightly higher than that in the turbulent region. There are two different entrainment mechanisms in turbulent FSL flow, namely, entrainment by engulfment in the transition region and by nibbling in the turbulent area (Mathew & Basu 2002; Jahanbakhshi & Madnia 2016). The results of figure 16(*a*) indicate that compared with entrainment by nibbling, entrainment by engulfment may yield higher mass entrainment ratio. After the R_M estimated by (3.9) reaches a maximum at $x \approx 350$, where the flow turns into turbulence, the magnitude of R_M by (3.9) gradually matches with the asymptotic value estimated by (3.10). In the turbulent area, the entrainment ratio is relatively steady, and the mass, momentum and energy are mainly entrained by nibbling. The mass flux entrainment from the high-speed side is significantly more than that from the low-speed side, leading to the momentum difference across the shear layer in the cross-stream direction, therefore causing the bending.

We have concluded that the asymmetric entrainment leads to the shear-layer bending. In this context, we further investigate this bending by the estimation of the bending angle. Dimotakis (1986) proposed a method to estimate the angle between the upper edge and the x-axis of the shear layer, indicated by α_1, and the angle between the lower edge and the x-axis, denoted by α_2. The corresponding angles are also demonstrated in figure 16(*b*). Angles α_1 and α_2 can be estimated by (Dimotakis 1986)

$$\frac{1 + R}{1 - R} \left(\frac{\tan \alpha_1}{\tan \alpha_2 + \tan \beta} \right) = R_M, \tag{3.11}$$

$$\tan \alpha_1 + \tan \alpha_2 = \frac{\mathrm{d}\delta_{vis}}{\mathrm{d}x}, \tag{3.12}$$

where $\tan \beta = V_2/U_2$ and V_2 is the cross-stream component of the low-speed mean velocity at the shear layer edge. Here δ_{vis} is the visual thickness and has been suggested
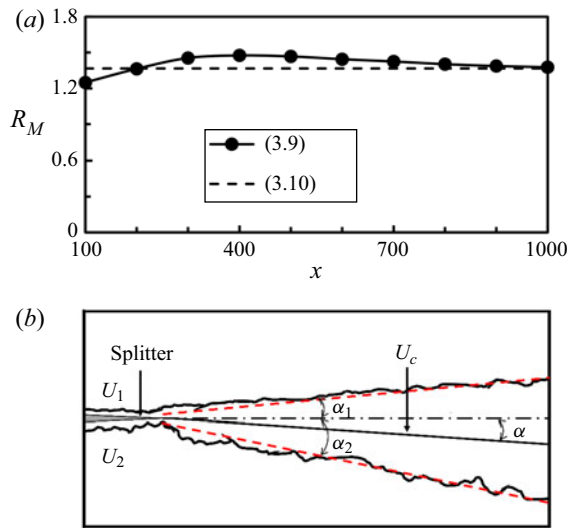
FIGURE 16. (*a*) Mass flux entrainment ratios estimated by (3.9) and (3.10) for $M_c = 0.3$ and (*b*) shear layer and bending angle schematic.

to be approximately two times the vorticity thickness δ_w (Brown & Roshko 1974). Thus, (3.12) can be modified as

$$\frac{1}{2}(\tan \alpha_1 + \tan \alpha_2) = \frac{\mathrm{d}\delta_w}{\mathrm{d}x}. \tag{3.13}$$

After obtaining angles α_1 and α_2, the bending angle α can be calculated by

$$\alpha = \frac{1}{2}(\alpha_2 - \alpha_1). \tag{3.14}$$

Conversely, using the current results shown in figure 14(*a*), we can estimate the angles α_1 and α_2, which can be used to calculate α and R_M by employing (3.14) and (3.11), respectively, for different M_c. The results are tabulated in table 3. Through data fitting, the data in table 3 can be used to modify (3.10) for the R_M estimation of the compressible planar FSL flow, i.e.

$$R_M = 1 + 0.46R + 0.18M_c + 0.08M_c^2, \tag{3.15}$$

for $M_c \leqslant 0.7$, due to the limited convective Mach numbers used in this work. Furthermore, we can use the angles in table 3 to verify (3.13). The vorticity thickness growth rates are calculated as 0.058, 0.055 and 0.051 for $M_c = 0.3$, 0.5 and 0.7, respectively, from (3.13). The computed results have excellent agreements with the corresponding results, 0.060, 0.055 and 0.050, estimated by $\mathrm{d}\delta_w/\mathrm{d}x$ with $\delta_w = \Delta U/(\mathrm{d}\{u\}/\mathrm{d}y)_{max}$. This confirms that, for the conditions considered in this study, (3.13) can accurately predict the relation between angles α_1 and α_2 with the vorticity growth rate.

The asymmetric entrainment in the turbulent region is also reflected from the cross-stream profiles of kinetic energy budget terms, such as kinetic energy convection and transport terms. Brown & Roshko (1974) proposed that entrainment is composed of three mechanisms: mean velocity engulfment, turbulent convection and turbulent transport; and the entrainment includes mass, momentum and energy entrainment. In the transition regions, the engulfment is the dominant mechanism for entrainment. In contrast,

M_c	α_1	α_2	α	R_M
0.3	2.20	4.38	1.09	1.30
0.5	2.00	4.30	1.15	1.37
0.7	1.75	4.11	1.18	1.41

TABLE 3. Shear-layer bending angles in degrees for $M_c = 0.3$, 0.5 and 0.7.
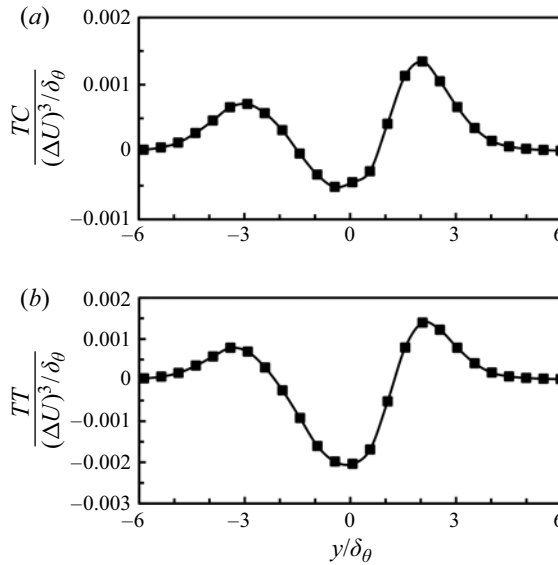

FIGURE 17. Cross-stream profiles of the normalized (*a*) turbulent convection and (*b*) turbulent transport at $x - x_E = 300$ in the turbulent region for $M_c = 0.3$. All terms are normalized by $(\Delta U)^3/\delta_\theta$.

the turbulent convection and transport are the leading mechanisms in the turbulent region (Brown & Roshko 1974). The turbulent convection (*TC*), $\partial \langle \rho \rangle \{u_k\}\{k\}/\partial x_k$, is the first term of (3.1), while the turbulent transport (*TT*) is

$$TT = -\frac{\partial \langle \rho \rangle \{u_k'' k''\}}{\partial x_k} - \frac{\partial \langle p' u_k' \rangle}{\partial x_k} + \frac{\partial \langle \tau_{ik}' u_i' \rangle}{\partial x_k}, \qquad (3.16)$$

where $\partial \langle \rho \rangle \{u_k'' k''\}/\partial x_k$, $\partial \langle p' u_k' \rangle/\partial x_k$ and $-\partial \langle \tau_{ik}' u_i' \rangle/\partial x_k$ are the second, third and fourth terms on the RHS of (3.1). Turbulent convection and transport play crucial roles in the lateral and longitudinal transport of mass, momentum and energy. Figures 17(*a*) and 17(*b*) show the cross-stream profiles of the turbulent convection and transport at $x - x_E = 300$ in the turbulent region for $Mc = 0.3$. The kinetic energy from the free streams entrains into the shear layer often through two regions. One region is laterally above the centre of the shear layer, between the high-speed free stream and the upper shear layer; another region is laterally below the shear layer, between the low-speed free stream and the lower shear layer. Both turbulent convection and turbulent transport profiles are double peaked, and the peaks are located in the two regions mentioned above. Note that the gain of the kinetic energy by convection and transport from the high-speed side outweighs that from
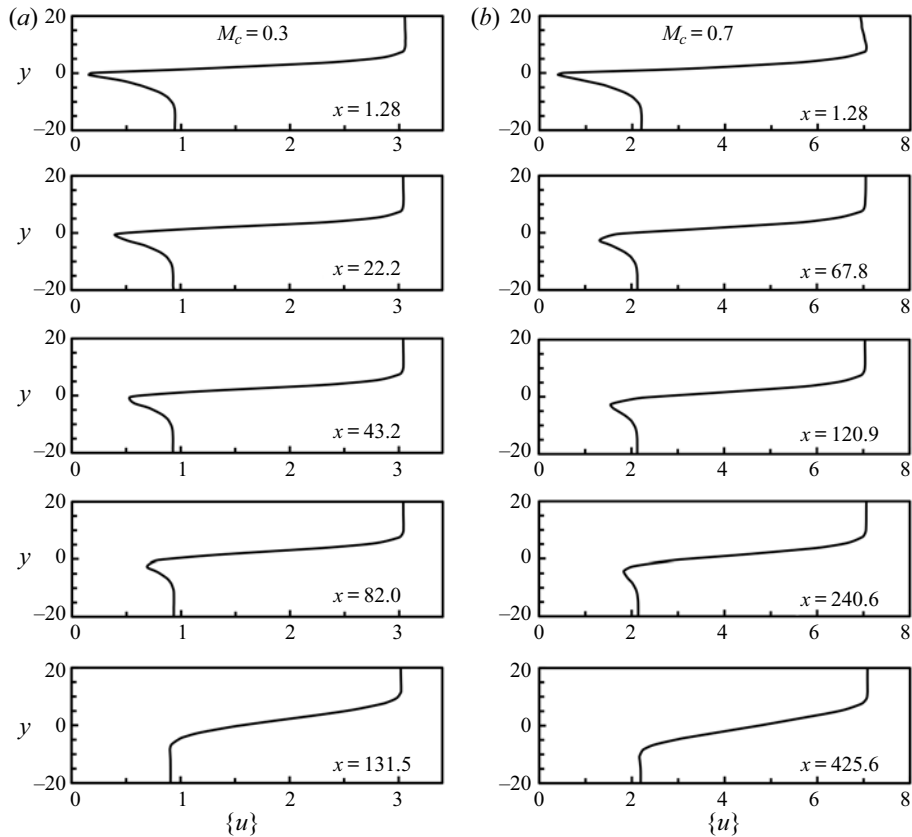
FIGURE 18. Cross-stream profiles of the streamwise Favre-averaged velocity at five streamwise locations for (*a*) $M_c = 0.3$ and (*b*) $M_c = 0.7$.

the low-speed side. This again demonstrates the asymmetric entrainment from the edges of the shear layer.

It is worth noting that, in figure 14(*b*), in the region $x < 150$, the lateral position of U_c locates at $y \approx 2.5$, rather than $y \approx 0$. This higher position is due to the rise of the velocity deficit. In the experiment, boundary layers develop along two sides of the splitter plate, then meet at the trailing edge, resulting in a velocity deficit. In this work, the velocity deficit in the shear layer follows two laminar boundary layers along the two sides of the splitter. In other words, two laminar boundary layers meet at the trailing edge while maintaining their laminar flow behaviours due to the inertia of the fluid. As a result, a layer of fluid with near-zero velocity (stagnation area) is formed downstream of the trailing edge. The cross-stream Favre-averaged velocity profiles of the shear layer are presented in figure 18 for five selected locations. We can see how the confluence initially results in a velocity deficit that decreases in the streamwise direction. The flow eventually evolves into a self-similar shear layer.

For the case with $M_c = 0.3$ in figure 18(*a*), the velocity deficit is observable up to $x = 131.5$ downstream of the trailing edge, beyond which the flow displays the features of a classical FSL. An estimate of the velocity deficit magnitude with downstream distance is shown in table 4. The velocity deficit, U_d, is calculated as

$$U_d = \left(U_{erf}\right)_c - \{u\}_{min}, \tag{3.17}$$

Downstream distance	Minimum velocity	Velocity deficit
1.279	0.1547	0.7487
22.18	0.3961	0.5073
43.18	0.5319	0.3715
82.04	0.6884	0.2150
131.5	0.9027	0.0007

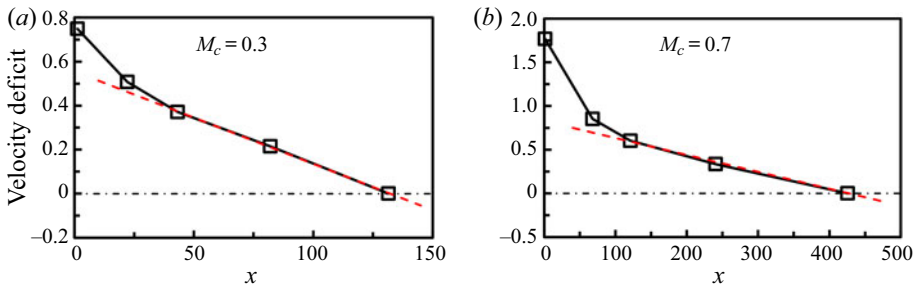TABLE 4. Velocity deficit with downstream distance for $M_c = 0.3$.

FIGURE 19. Evolution of the velocity deficit along the streamwise direction for (*a*) $M_c = 0.3$ and (*b*) $M_c = 0.7$. The red dashed line is the added trendline for each case.

where $(U_{erf})_c$ is the velocity at the centre ($y = y_{0.5}$) of the classical error function profile, and $\{u\}_{min}$ is the minimum velocity of the cross-stream profile of the streamwise Favre-averaged velocity from the current study. The classical error function profile was derived by Gortler (1942), assuming constant viscosity and density across the shear layer, defined as

$$U_{erf} = U_2 + \frac{\Delta U}{2}[1 + \mathrm{erf}(\eta)]. \tag{3.18}$$

Here, η is the similarity variable, expressed as

$$\eta = \frac{(y - y_{0.5})}{(x - x_0)}, \tag{3.19}$$

where x_0 is the origin of the FSL. The data in table 4 can be extrapolated to predict that the velocity deficit should disappear approximately at $x = 132$ after the confluence, also demonstrated in figure 19(*a*). Similarly, we calculate the velocity deficit for $M_c = 0.7$, shown in figure 18(*b*) and tabulated in table 5. Again, we can predict that the classic shear-layer profile can be recovered approximately at $x = 428$, presented in figure 19(*b*) as well. For convenience, we call the distance between the initial emergence and the final disappearance of the velocity deficit the VDPD. Furthermore, based on the trend observed in figure 19, we can deduce that the VDPD increases as the convective Mach number increases.

To examine the energy contributions of budget terms in the cross-stream direction, we compare the normalized $\mathcal{P}$, ε, Φ, Π and Ψ at the lower edge ($y = -62.45$), centre and upper edge ($y = 41.47$) of the shear layer at $x - x_E = 300$ in the turbulent region, shown

Downstream distance	Minimum velocity	Velocity deficit
1.279	0.3982	1.7677
67.84	1.3128	0.8531
120.9	1.5631	0.6028
240.6	1.8313	0.3346
425.6	2.1651	0.0008

TABLE 5. Velocity deficit with downstream distance for $M_c = 0.7$.
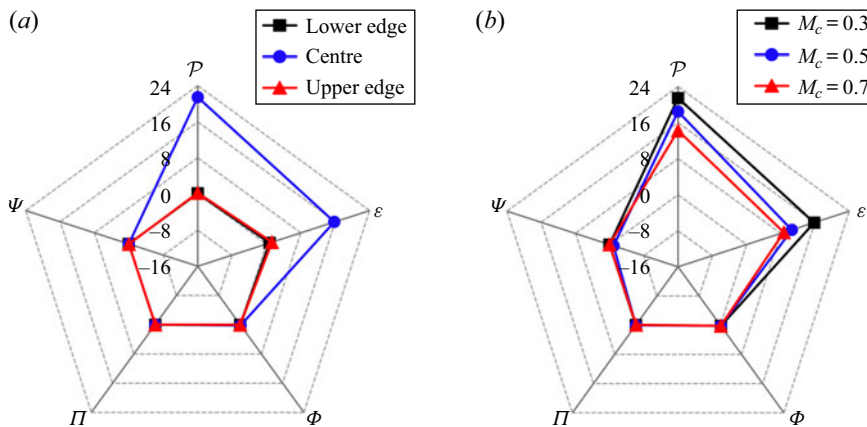
FIGURE 20. Comparisons of $\mathcal{P}$, ε, Φ, Π and Ψ, (a) at the lower edge ($y = -62.45$), centre and upper edge ($y = 41.47$) of the shear layer for $M_c = 0.3$, (b) at the centre of the shear layer for $M_c = 0.3$, 0.5 and 0.7, at $x - x_E = 300$ in turbulent region. All terms are normalized by $(\Delta U)^3 / \delta_\theta \times 10^{-4}$.

in figure 20(a). At the lower and upper edges of the shear layer, the magnitudes of all normalized terms are near zero, while at the shear layer centre, the turbulent production and turbulent viscous dissipation have considerable contributions to the energy exchange. Note that the ratio of $\mathcal{P}$ to ε at the centre of the shear layer is approximately 1.3. This near unity ratio indicates that in the turbulent region, the energy contribution of the turbulent viscous dissipation almost overtakes that of the turbulent production; hence the growth rate of the kinetic energy gradually decreases. Figure 20(b) compares the magnitudes of the five normalized terms for different M_c at the centre of the shear layer. We can see that the normalized $\mathcal{P}$ and ε significantly decrease with increasing M_c, whereas the other terms show only small changes, due to the employed scale and their relatively small energy contributions.

The evolutions of the normalized $\mathcal{P}^I$, ε^I, Φ^I, Π^I and Ψ^I in the turbulent region are shown in figure 21. The magnitudes of the five normalized terms decay gradually to asymptotic values, due to the turbulent viscous dissipation and the shear layer cross-stream diffusion. With increasing M_c, the normalized $\mathcal{P}^I$ and ε^I decrease, as shown in figures 21(a) and 21(b), due to the reductions of Reynolds stresses and velocity fluctuations, respectively. In the turbulent region, the value of Φ^I becomes very small (see figure 21c), meaning that most large vortex structures have turned into small
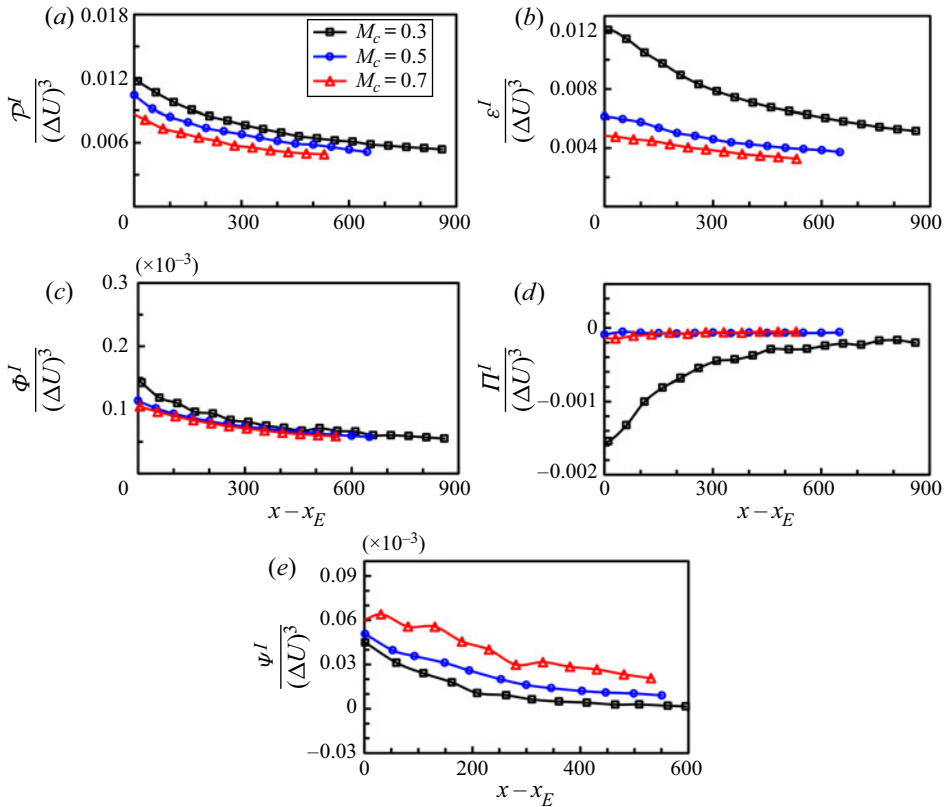
FIGURE 21. Evolution of the cross-stream integrals (*a*) $\mathcal{P}^I$, (*b*) ε^I, (*c*) Φ^I, (*d*) Π^I and (*e*) Ψ^I for $M_c = 0.3$, 0.5 and 0.7 in turbulent region. All terms are normalized by $(\Delta U)^3$.

vortex structures. Also, the value of Φ^I is not significantly affected by compressibility. This is attributed to the insensitive mean velocity field with respect to the change of M_c. In contrast, the normalized value of Ψ^I increases with increasing M_c (see figure 21*e*), owing to the sensitive cross-stream pressure gradient with respect to compressibility. Figure 21(*d*) shows that the normalized value of Π^I decreases significantly from $M_c = 0.3$ to 0.5, while remains almost the same from $M_c = 0.5$ to 0.7. As the flow advances downstream, the magnitudes of the normalized Π^I for all cases become very close to zero, suggesting that the contribution of the pressure dilatation to the TKE is insignificant. This is attributed to the self-cancellation of temporal oscillations when averaging the instantaneous pressure dilatation, $p'(\partial u'_k / \partial x_k)$ over time. Thus, we examine the importance of $p'(\partial u'_k / \partial x_k)$, instead.

The evolution of $p'(\partial u'_k / \partial x_k)$ at a typical location $(x - x_E, y, z) = (300, -6.5, 40)$ is presented as a function of flow-through-time and compared with the budget term turbulent production, shown in figure 22. The flow-through-time is defined as the time required for the flow to travel from the inlet to the outlet with the convective velocity, i.e.

$$\text{flow-through-time} = \frac{L_x}{U_c}. \tag{3.20}$$

From figure 22, we can see that $p'(\partial u'_k / \partial x_k)$ develops oscillations in time with relatively large amplitudes; its negative and positive extrema are nearly symmetric; the magnitude of
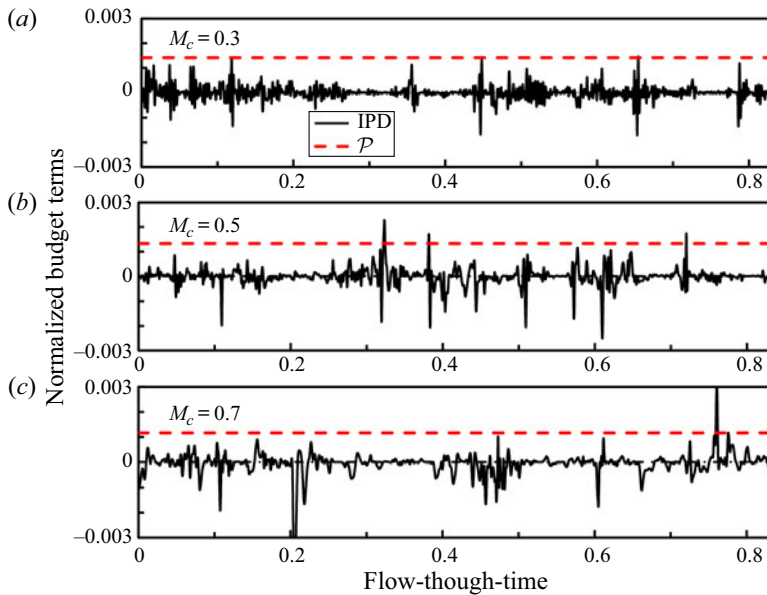
FIGURE 22. Evolution of the instantaneous pressure dilatation (known as IPD) and the turbulent production at $x - x_E = 300$, $y = -6.5$ and $z = 40$ in the self-similar turbulent region, normalized by $(\Delta U)^3/\delta_\theta$.

its extremum increases from 1.08×10^{-4} to 1.47×10^{-4} and 3.11×10^{-4} as M_c increases from 0.3 to 0.5 and 0.7. The fluctuations of the pressure dilatation are also comparable to the value of turbulent production. Thus, the fluctuations of pressure dilatation have a significant contribution to the evolution of TKE, and increase in magnitude with increasing M_c.

The effect of compressibility on the fluctuations of pressure dilatation is also evidenced by a marked difference in the probability density functions (p.d.f.s) of the normalized instantaneous pressure dilatation. The p.d.f.s at $x - x_E = 300$, $y = -6.5$ and $z = 40$ in the self-similar turbulent region for cases with $M_c = 0.3$, 0.5 and 0.7 are presented in figure 23. In all cases, the expected exponential roll-off of the p.d.f. is obvious. However, the p.d.f. from the high convective Mach number case is slightly less symmetric about zero. The right- and left-hand tails of the p.d.f. become longer with increasing convective Mach number, suggesting that the range of the pressure-dilatation fluctuations increases monotonically with M_c, which is consistent with the conclusion from figure 22. Note that the increased range of fluctuations is smaller as M_c increases from 0.5 to 0.7, compared with that from 0.3 to 0.5. Moreover, the peak of the p.d.f. at zero is more pronounced in the low convective Mach number cases, implying that more small values of pressure-dilatation fluctuations are present in such cases. The impact of compressibility on turbulent production and dissipation terms are further examined in the next section by analysing their components.

3.3. *Components of turbulent production and viscous dissipation*

The previous section shows that the turbulent production and viscous dissipation make the most significant contributions to the energy exchange among TKE, MKE and MIE. To further investigate the compressibility effects on the energy exchange in the shear layer,
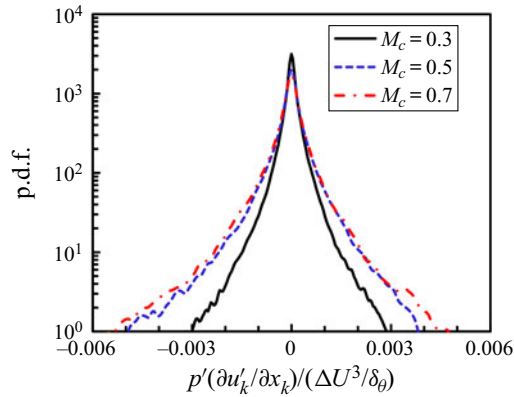
FIGURE 23. Probability density functions of instantaneous pressure dilatation at $x - x_E = 300$, $y = -6.5$ and $z = 40$ in the self-similar turbulent region, normalized by $(\Delta U)^3/\delta_\theta$.

we decompose these terms and analyse their components and the compressibility effects on them. The turbulent production term can be decomposed into

$$
\mathcal{P} = -\langle\rho\rangle\{u''u''\}\frac{\partial\{u\}}{\partial x} - \langle\rho\rangle\{v''v''\}\frac{\partial\{v\}}{\partial y} - \langle\rho\rangle\{w''w''\}\frac{\partial\{w\}}{\partial z} - \langle\rho\rangle\{u''v''\}\frac{\partial\{u\}}{\partial y}
$$

$$
- \langle\rho\rangle\{u''w''\}\frac{\partial\{u\}}{\partial z} - \langle\rho\rangle\{v''u''\}\frac{\partial\{v\}}{\partial x} - \langle\rho\rangle\{v''w''\}\frac{\partial\{v\}}{\partial z} - \langle\rho\rangle\{w''u''\}\frac{\partial\{w\}}{\partial x}
$$

$$
- \langle\rho\rangle\{w''v''\}\frac{\partial\{w\}}{\partial y}. \tag{3.21}
$$

Here, the third, fifth, seventh, eighth and ninth terms on the RHS of (3.21) are negligible since the current shear layer is statistically homogeneous in the spanwise direction. Consequently, the expression for turbulent production can be reduced to

$$
\mathcal{P} \approx \underbrace{-\langle\rho\rangle\{u''u''\}\frac{\partial\{u\}}{\partial x}}_{\mathcal{P}_1} \underbrace{-\langle\rho\rangle\{v''v''\}\frac{\partial\{v\}}{\partial y}}_{\mathcal{P}_2} \underbrace{-\langle\rho\rangle\{u''v''\}\frac{\partial\{u\}}{\partial y}}_{\mathcal{P}_3} \underbrace{-\langle\rho\rangle\{v''u''\}\frac{\partial\{v\}}{\partial x}}_{\mathcal{P}_4}. \tag{3.22}
$$

For brevity, $-\langle\rho\rangle\{u''u''\}\partial\{u\}/\partial x$, $-\langle\rho\rangle\{v''v''\}\partial\{v\}/\partial y$, $-\langle\rho\rangle\{u''v''\}\partial\{u\}/\partial y$ and $-\langle\rho\rangle\{v''u''\}\partial\{v\}/\partial x$ are referred to as $\mathcal{P}_1$, $\mathcal{P}_2$, $\mathcal{P}_3$ and $\mathcal{P}_4$, respectively. The cross-stream variations of these terms are shown in figure 24 for various M_c. The dominant component in the turbulent production equation, (3.22), is $\mathcal{P}_3$, indicating that the planar FSL behaves statistically as a 2-D flow, as shown in the previous studies. Thus, as M_c increases, the decrease of the normalized turbulent production is attributed to the reduction of $\mathcal{P}_3$. On the other hand, the normalized $\{u\}$ is not considerably affected by compressibility. Hence, the reduction of $\mathcal{P}_3$ is mainly due to the reduction of $\{u''v''\}$, which is demonstrated in figure 25. Vreman *et al.* (1996) showed that the growth rate of a temporal mixing layer is proportional to the integrated turbulence production component, $\mathcal{P}_3^I$, in the fully developed turbulent region. In a temporally evolving plane FSL, such relation can be expressed as
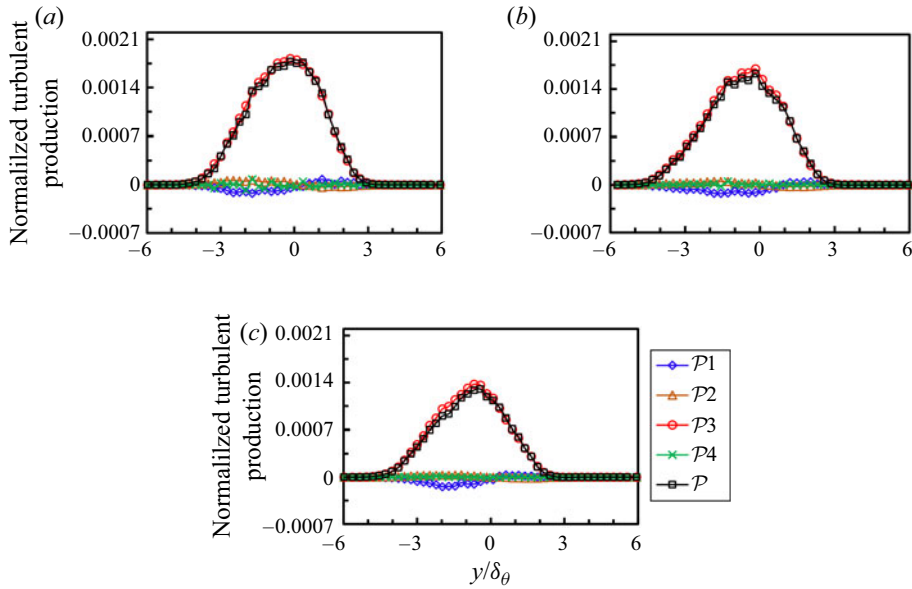
FIGURE 24. Cross-stream profiles of the normalized turbulent production and its significant components for (*a*) $M_c = 0.3$, (*b*) $M_c = 0.5$ and (*c*) $M_c = 0.7$ at $x - x_E = 300$ in the turbulent region and normalized by $(\Delta U)^3/\delta_\theta$.
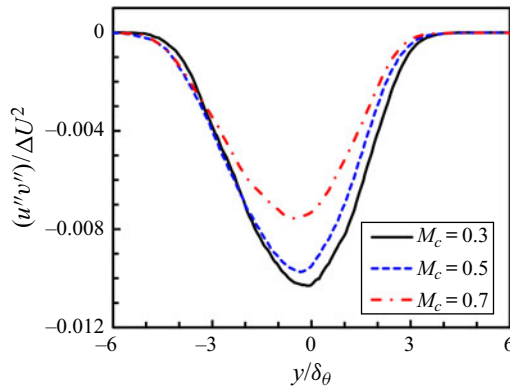

FIGURE 25. Comparison of the normalized $\{u''v''\}$ profiles at $x - x_E = 300$ in turbulent region for different convective Mach numbers.

(Vreman *et al.* 1996)

$$\frac{d\delta_\theta}{dt} = -\frac{2}{\rho_o(\Delta U)^2} \int_{-\infty}^{+\infty} \langle \rho \rangle \{u''v''\} \frac{\partial \{u\}}{\partial y} dy. \tag{3.23}$$

Combining (3.8) with (3.23), the relation between the temporal growth rate and turbulent production is further simplified to

$$\frac{d\delta_\theta}{dt} = \frac{2\mathcal{P}_3^I}{\rho_o(\Delta U)^2}. \tag{3.24}$$

The relation between the momentum thickness growth rates of temporally and spatially developing FSLs can be expressed as (Brown & Roshko 1974)

$$\frac{d\delta_\theta}{dt} = \frac{\Delta U}{2R} \frac{d\delta_\theta}{dx}. \tag{3.25}$$

Then, the corresponding momentum thickness growth rate of a spatially developing FSL in the turbulent region becomes

$$\frac{d\delta_\theta}{dx} = \frac{4R\mathcal{P}_3^I}{\rho_o (\Delta U)^3}. \tag{3.26}$$

It is clear that the growth rate of a spatial FSL is proportional to the integrated turbulence production component, $\mathcal{P}_3^I$, and the growth rate can be calculated from (3.26). At $x - x_E = 300$ in the turbulent region, the normalized integral of turbulent production is $\mathcal{P}_3^I/(\Delta U)^3 = 0.00641$, 0.00581 and 0.00495 for $M_c = 0.3$, 0.5 and 0.7, respectively. Consequently, the momentum thickness growth rates are $d\delta_\theta/dx = 0.0138$, 0.0125 and 0.0107 by employing (3.26). These results have excellent agreements with the corresponding results, $d\delta_\theta/dx = 0.0137$, 0.0121 and 0.0106, listed in table 2 computed using (2.17). This suggests that, for the conditions considered in this study, temporal simulation is capable of predicting the compressible FSL growth rate, despite the fact that temporal simulation possesses some significant drawbacks for simulating turbulent FSL, such as the lack of ability in capturing the effects of the velocity ratio across the FSL and the asymmetry of entrainment (Ho & Huerre 1984; Hussaini & Voigt 1990; Lui & Lele 2001; Pickett & Ghandhi 2002; Fu & Li 2006).

Besides the dominant component $\mathcal{P}_3$, the component $\mathcal{P}_1$ shows noticeable variations across the shear layer in figure 24. The value of $\mathcal{P}_1$ is negative in the low-speed side of the shear layer and slightly positive in the high-speed side. Note that $\{u''u''\}$ is always positive, thus, does not affect the sign of $\mathcal{P}_1$. The sign of $\mathcal{P}_1$ is determined by $\partial\{u\}/\partial x$. Note that a negative value of $\partial\{u\}/\partial x$ means a compression in the streamwise direction while a positive value does the opposite. Consequently, fluid elements in the low- and high-speed sides experience compression and expansion, respectively. This is a further evidence of the commonly recognized phenomenon that the mixing layer bends towards the side with lower speed. Furthermore, the value of $\mathcal{P}_1$ is almost unaffected by the change of M_c. As mentioned above, $\{u\}$ is nearly not influenced by compressibility. Based on the result from part I, $\{u''u''\}$ is not sensitive to the change of M_c either. Therefore, $\mathcal{P}_1$ is not a function of M_c.

The compressibility effect on the turbulent viscous dissipation term is also further investigated by considering its components (Huang *et al.* 1995),

$$\varepsilon \equiv \left\langle \tau'_{ik} \frac{\partial u'_i}{\partial x_k} \right\rangle = \varepsilon_1 + \varepsilon_2 + \varepsilon_3, \tag{3.27}$$

where

$$\varepsilon_1 = \langle\mu\rangle \left\langle \frac{\partial u'_i}{\partial x_k} \left(\frac{\partial u'_i}{\partial x_k} + \frac{\partial u'_k}{\partial x_i} \right) \right\rangle - \frac{2}{3} \langle\mu\rangle \left\langle \frac{\partial u'_i}{\partial x_k} \frac{\partial u'_l}{\partial x_l} \right\rangle \delta_{ik}, \tag{3.28}$$

$$\varepsilon_2 = \left\langle \mu' \frac{\partial u'_i}{\partial x_k} \left(\frac{\partial u'_i}{\partial x_k} + \frac{\partial u'_k}{\partial x_i} \right) \right\rangle - \frac{2}{3} \left\langle \mu' \frac{\partial u'_i}{\partial x_k} \frac{\partial u'_l}{\partial x_l} \right\rangle \delta_{ik}, \tag{3.29}$$

$$\varepsilon_3 = \left\langle \mu' \frac{\partial u'_i}{\partial x_k} \right\rangle \left(\frac{\partial \langle u_i \rangle}{\partial x_k} + \frac{\partial \langle u_k \rangle}{\partial x_i} \right) - \frac{2}{3} \left\langle \mu' \frac{\partial u'_i}{\partial x_k} \right\rangle \frac{\partial \langle u_l \rangle}{\partial x_l} \delta_{ik}. \tag{3.30}$$
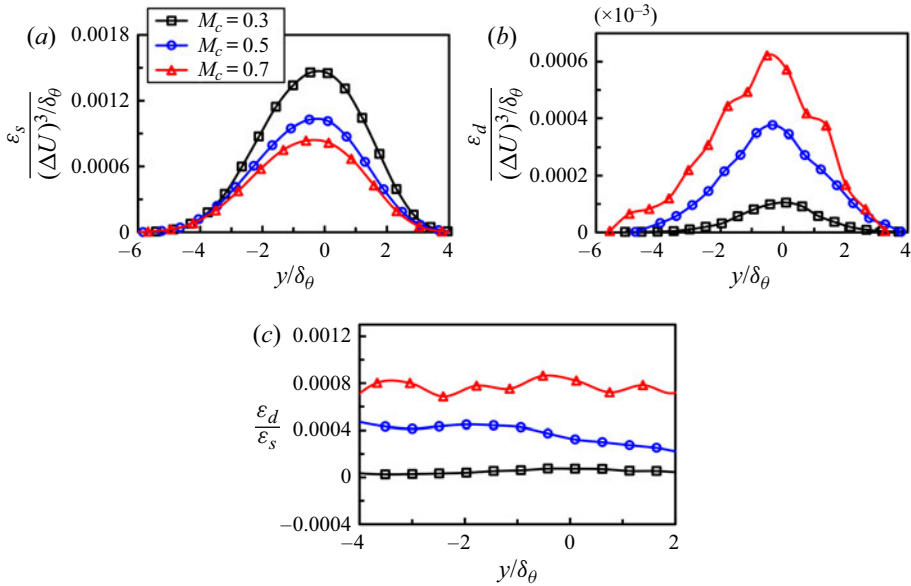
FIGURE 26. Cross-stream profiles of (*a*) normalized solenoidal dissipation, $\varepsilon_s/((\Delta U)^3/\delta_\theta)$, (*b*) normalized dilatational dissipation, $\varepsilon_d/((\Delta U)^3/\delta_\theta)$. (*c*) Ratios of dilatational dissipation to solenoidal dissipation, $\varepsilon_d/\varepsilon_s$, as a function of y/δ_θ at $x - x_E = 300$.

When fluctuations in viscosity are neglected, only ε_1 is significant. This term can be decomposed into solenoidal dissipation, ε_s, dilatational dissipation, ε_d, and inhomogeneous dissipation, ε_I,

$$\varepsilon \approx \varepsilon_1 = \varepsilon_s + \varepsilon_d + \varepsilon_I, \tag{3.31}$$

where

$$\varepsilon_s = 2\langle\mu\rangle\langle\omega'_{ij}\omega'_{ij}\rangle, \tag{3.32}$$

$$\varepsilon_d = \frac{4}{3}\langle\mu\rangle\left\langle\frac{\partial u'_l}{\partial x_l}\frac{\partial u'_k}{\partial x_k}\right\rangle, \tag{3.33}$$

$$\varepsilon_I = 2\langle\mu\rangle\left(\frac{\partial^2\langle u'_i u'_j\rangle}{\partial x_i \partial x_j} - 2\frac{\partial}{\partial x_i}\left\langle u'_i \frac{\partial u'_j}{\partial x_j}\right\rangle\right), \tag{3.34}$$

with

$$\omega'_{ij} = \frac{1}{2}\left(\frac{\partial u'_i}{\partial x_j} - \frac{\partial u'_j}{\partial x_i}\right). \tag{3.35}$$

Figures 26(*a*) and 26(*b*) show the normalized cross-stream profiles of the solenoidal dissipation and the dilatational dissipation, respectively, as a function of y/δ_θ at $x - x_E = 300$ in the turbulent region for all three cases. The magnitude of the normalized solenoidal dissipation decreases with increasing M_c, while the normalized dilatational dissipation shows the opposite trend. Figure 26(*c*) presents the ratio of the dilatational dissipation to the solenoidal dissipation in the same location, which reveals the following findings: the dilatational dissipation is approximately three orders of magnitude smaller than the solenoidal dissipation for $M_c = 0.5$ and 0.7; for $M_c = 0.3$, the magnitude of

the dilatational dissipation is nearly four orders of magnitude smaller than that of the solenoidal dissipation; the ratio of the dilatational dissipation to the solenoidal dissipation increases as the M_c increases. For the convective Mach numbers used in the present study, the dilatational dissipation seems to play an insignificant role in the TKE budget. This conclusion is consistent with the temporal simulation results by Blaisdell & Zeman (1992) and Vreman *et al.* (1996). The inhomogeneous dissipation component results from the shear between the shear layer (parallel to the wall) and the wall (Lele 1994; Huang *et al.* 1995; Cadiou, Hanjalic & Stawiarski 2004; Brown *et al.* 2017). Thus, inhomogeneous dissipation approaches zero when far away from the wall. As expected, the inhomogeneous dissipation term is near zero in the turbulent region based on the current DNS results. Therefore, the inhomogeneous dissipation has insignificant contribution to the energy exchange between TKE and MIE.

4. Summary and conclusions

Direct numerical simulations have been conducted using a high-order DSEM for a 3-D, spatially developing compressible plane FSL. The shear layer is formed by two parallel streams, under naturally developing inflow condition and separated by a splitter plate. The initial momentum thickness Reynolds number is set to 140 for convective Mach numbers of 0.3, 0.5 and 0.7.

A large buffer zone surrounds the large computational domain. Consequently, the FSL flow can reach the self-similar turbulent state in the streamwise direction and can grow freely in the cross-stream and spanwise directions. The buffer zone prevents solution contamination from the boundaries. Within the shear layer, the average grid size is smaller than those used by Pantano & Sarkar (2002) and Zhou *et al.* (2012) in their DNS studies. The resolution of the current grid is sufficient to accurately calculate all relevant turbulent scales and energy budget terms. A detailed validation against published theoretical, experimental and numerical results is performed and found to agree well with the convective Mach numbers used in this work (see part I of this work).

The energy exchanges among TKE, MKE and MIE are examined, and the effects of compressibility on such exchanges are assessed. By considering the transport equations of TKE, MKE and MIE, the roles of different budget terms in the energy transfer are identified. It is confirmed that the energy exchange between TKE and MKE is through turbulent production and enthalpic production terms (Lele 1994). With increasing compressibility, the energy exchange from MKE to TKE through turbulent production decreases, while the enthalpic production that converts energy from TKE to MKE increases. The contribution of enthalpic production is smaller than that of turbulent production. The component, $-\langle\rho\rangle\{u''v''\}\partial\{u\}/\partial y$, of turbulent production is the dominant one, and is mainly responsible for the decrease in turbulent production with increasing convective Mach number, as previously reported by Vreman *et al.* (1996).

Turbulent viscous dissipation and pressure-dilatation terms are responsible for the energy exchange between TKE and MIE. Increasing the compressibility decreases the energy exchange from TKE to MIE through turbulent viscous dissipation and pressure dilatation. Among the components of the turbulent viscous dissipation, the dilatational dissipation is approximately three orders of magnitude smaller than the solenoidal dissipation for $M_c = 0.5$ and 0.7, and nearly four orders of magnitude for $M_c = 0.3$. The ratio of the dilatational dissipation to the solenoidal dissipation increases as the M_c increases. For the convective Mach numbers used in the present study, the

dilatational dissipation is insignificant in the TKE budget, as previously shown by Blaisdell & Zeman (1992) and Vreman *et al.* (1996) in the temporal simulations.

Pressure dilatation contribution to energy exchange is small compared with that of turbulent viscous dissipation. However, the fluctuations of pressure dilatation are relatively large and comparable to the magnitudes of turbulent production and viscous dissipation at the same location. The p.d.f.s of the normalized instantaneous pressure dilatation show that the range of the pressure-dilatation fluctuations increases monotonically with convective Mach number. The energy exchange between MKE and MIE is mainly through mean viscous dissipation. The mean viscous dissipation has a positive sign and always converts energy from MKE to MIE. Also, the normalized mean viscous dissipation is nearly insensitive to the change of convective Mach number.

The variations of the five budget terms in the cross-stream direction are also analysed. For the turbulent production, turbulent viscous dissipation, mean viscous dissipation and turbulent pressure dilatation, their peaks are located near the centre of the shear layer, while enthalpic production shows two peaks near the edges of the shear layer and a valley at the centre, mainly due to the variation of the mean pressure gradient with respect to cross-stream direction. We show that the cross-stream profiles of the turbulent production and turbulent viscous dissipation noticeably shift to the low-speed side of the shear layer. This bending of the shear layer is only captured in the spatially evolving turbulent shear layer simulations. In this work, the bending behaviour is explained quantitatively in terms of the asymmetry mass flux entrainment of the shear layer. The mass flux entrainment from the high-speed side is more than that from the low-speed side, leading to the momentum difference across the shear layer in the cross-stream direction, hence causing the shear-layer bending. The bending angle estimation for the compressible shear layer is also introduced.

The evolutions of the cross-stream integrals of the five budget terms are examined. The profiles of turbulent production for $M_c = 0.3$ and 0.5, appear to have a double-peak variation, due to the emergence of the first and second pairings. With increasing M_c to 0.7, the double-peak variation turns into single peak. This is attributed to the appearance of the streamwise elongated vortex structures, which have less tendency to roll and pair in the streamwise direction. The cross-stream integrals of the five budget terms in the transition region are more sensitive to the change of M_c than that in the turbulent area. In the turbulent region, the magnitudes of the integrals decay gradually to asymptotic values, due to the turbulent dissipation and the cross-stream diffusion.

Declaration of interests

The authors report no conflict of interest.

REFERENCES

ATOUFI, A., FATHALI, M. & LESSANI, B. 2015 Compressibility effects and turbulent kinetic energy exchange in temporal mixing layers. *J. Turbul.* **16**, 676–703.

BIRCH, S. F. & EGGERS, J. M. 1972 A critical review of the experimental data for developed free turbulent shear layers. *NASA Tech. Rep.* SP 321. National Aeronautics and Space Administration.

BLAISDELL, G. A., COLEMAN, G. N. & MANSOUR, N. N. 1996 Rapid distortion theory for compressible homogeneous turbulence under isotropic mean strain. *Phys. Fluids* **8**, 2692–2705.

BLAISDELL, G. A., MANSOUR, N. N. & REYNOLDS, W. C. 1993 Compressibility effects on the growth and structure of homogeneous turbulent shear flows. *J. Fluid Mech.* **256**, 443–485.

BLAISDELL, G. A. & ZEMAN, O. 1992 Investigation of the dilatational dissipation in compressible homogeneous shear flow. In *Proceedings of the 1992 Summer Program, Center for Turbulence Research, Stanford/NASA Ames* (ed. P. Moin, W. C. Reynolds & J. Kim), pp. 231–245. Stanford University.

BODE, B., BUTLER, M., DUNNING, T., HOEFLER, T., KRAMER, W., GROPP, W. & HWU, W. 2013 The Blue Waters super-system for super-science. In *Contemporary High Performance Computing*, pp. 339–366. CRC Press.

BOGDANOFF, D. W. 1983 Compressibility effects in turbulent shear layers. *AIAA J.* **21**, 926–927.

BRADSHAW, P. 1966 The effect of initial conditions on the development of a free shear layer. *J. Fluid Mech.* **26**, 225–236.

BROWN, C. S., SHAVER, D. R., LAHEY, R. T. & BOLOTNOV, I. A. 2017 Wall-resolved spectral cascade-transport turbulence model. *Nucl. Sci. Engng* **320**, 309–324.

BROWN, G. L. & ROSHKO, A. 1974 On density effects and large structure in turbulent mixing layers. *J. Fluid Mech.* **64**, 775–816.

CADIOU, A., HANJALIC, K. & STAWIARSKI, K. 2004 A two-scale second-moment turbulence closure based on weighted spectrum integration. *Theor. Comput. Fluid Dyn.* **18**, 1–26.

CARPENTER, M. H. & KENNEDY, C. A. 1994 Fourth-order 2N-storage Runge–Kutta schemes. *NASA Tech. Rep.* TM 109112. National Aeronautics and Space Administration.

CHEN, J. H., CANTWELL, B. J. & MANSOUR, N. N. 1989 The effect of Mach number on the stability of a plane supersonic wake. *Phys. Fluids* A **2**, 984–1004.

CHEN, Z., YI, S., HE, L., TIAN, L. & ZHU, Y. 2012 An experimental study on fine structures of supersonic laminar/turbulent flow over a backward-facing step based on NPLS. *Chinese Sci. Bull.* **57**, 584–590.

CHU, B. T. & KOVASZNAY, L. S. G. 1958 Non-linear interaction in a viscous heat-conducting compressible gas. *J. Fluid Mech.* **3**, 494–514.

CLEMENS, N. T. & MUNGAL, M. G. 1995 Large-scale structure and entrainment in the supersonic mixing layer. *J. Fluid Mech.* **284**, 171–216.

CORRSIN, S. & KISTLER, A. 1955 Free-stream boundaries of turbulent flows. *NACA Tech. Rep.* TN 1244. National Advisory Committee for Aeronautics.

DAY, M. J., MANSOUR, N. N. & REYNOLDS, W. C. 2001 Nonlinear stability and structure of compressible reacting mixing layer. *J. Fluid Mech.* **446**, 375–408.

DAY, M. J., REYNOLDS, W. C. & MANSOUR, N. N. 1998 The structure of the compressible reacting mixing layer: insights from linear stability analysis. *Phys. Fluids* **10**, 993–1007.

DIMOTAKIS, P. E. 1986 Two-dimensional shear-layer entrainment. *AIAA J.* **24**, 1791–1796.

ELLIOTT, G. S. & SAMIMY, M. 1990 Compressibility effects in free shear layers. *Phys. Fluids* A **2**, 1231–1240.

ERLEBACHER, G., HUSSAINI, M. Y., KREISS, H. O. & SARKAR, S. 1990 The analysis and simulation of compressible turbulence. *Theor. Comput. Fluid Dyn.* **2**, 73–95.

FAVRE, A. 1965 The equations of compressible turbulent gases. Annual Summary Report AD0622097.

FAVRE, A. 1969 *Statistical Equations of Turbulent Gases. Problems of Hydrodynamics and Continuum Mechanics*, pp. 231–266. SIAM.

FOYSI, H. & SARKAR, S. 2010 The compressible mixing layer: an LES study. *Theor. Comput. Fluid Dyn.* **24**, 565–588.

FREUND, J. B., LELE, S. K. & MOIN, P. 2000 Compressibility effects in a turbulent annular mixing layer. Part 1. Turbulence and growth rate. *J. Fluid Mech.* **421**, 229–267.

FU, S. & LI, Q. 2006 Numerical simulation of compressible mixing layers. *Intl J. Heat Fluid Flow* **27**, 895–901.

GAO, Z. & MASHAYEK, F. 2004 Stochastic model for non-isothermal droplet-laden turbulent flows. *AIAA J.* **42**, 255–260.

GHIASI, Z., KOMPERDA, J., LI, D. & MASHAYEK, F. 2016 Simulation of supersonic turbulent non-reactive flow in ramp-cavity combustor using a discontinuous spectral element method. *AIAA Paper* 2016-0617.

GHIASI, Z., KOMPERDA, J., LI, D., PEYVAN, A., NICHOLLS, D. & MASHAYEK, F. 2019 Modal explicit filtering for large eddy simulation in discontinuous spectral element method. *J. Comput. Phys.* **3**, 100024.

GOEBEL, S. G. & DUTTON, J. C. 1991 Experimental study of compressible turbulent mixing layers. *AIAA J.* **29**, 538–546.

GORTLER, H. 1942 Berechnung von aufgaben der freien turbulenz auf grund eines neuen naherungsansatzes. *Z. Angew. Math. Mech.* **22**, 244–254.

GROSCH, C. E. & JACKSON, T. L. 1991 Inviscid spatial stability of a three-dimensional compressible mixing layer. *J. Fluid Mech.* **231**, 35–50.

HALL, J. L., DIMOTAKIS, P. E. & ROSEMANN, H. 1993 Experiments in non-reacting compressible shear layers. *AIAA J.* **31**, 2247–2254.

HAMBA, F. 1999 Effects of pressure fluctuations on turbulence growth in compressible shear flow. *Phys. Fluids* **11**, 1623–1635.

HO, C.-M. & HUANG, L.-S. 1982 Subharmonics and vortex merging in mixing layers. *J. Fluid Mech.* **119**, 443–473.

HO, C. M. & HUERRE, P. 1984 Perturbed free shear layers. *Annu. Rev. Fluid Mech.* **16**, 365–424.

HUANG, P. G., COLEMAN, G. N. & BRADSHAW, P. 1995 Compressible turbulent channel flows: DNS results and modelling. *J. Fluid Mech.* **305**, 185–218.

HUSSAINI, M. Y. & VOIGT, R. G. 1990 *Instability and Transition*. Springer.

JACKSON, T. L. & GROSCH, C. E. 1989 Inviscid spatial stability of a compressible mixing layer. *J. Fluid Mech.* **208**, 609–637.

JACOBS, G. B. 2003 Numerical simulation of two-phase turbulent compressible flows with a multidomain spectral method. PhD thesis, University of Illinois at Chicago, Chicago, IL.

JACOBS, G. B., KOPRIVA, D. A. & MASHAYEK, F. 2003 A comparison of outflow boundary conditions for the multidomain staggered-grid spectral method. *Numer. Heat Transfer* **44** (3), 225–251.

JACOBS, G. B., KOPRIVA, D. A. & MASHAYEK, F. 2004 Compressibility effects on the subsonic two-phase flow over a square cylinder. *J. Propul. Power* **20**, 353–359.

JACOBS, G. B., KOPRIVA, D. A. & MASHAYEK, F. 2005 Validation study of a multidomain spectral code for simulation of turbulent flows. *AIAA J.* **43**, 1256–1264.

JAHANBAKHSHI, R. & MADNIA, C. K. 2016 Entrainment in a compressible turbulent shear layer. *J. Fluid Mech.* **797**, 564–603.

JAVED, A., RAJAN, N. K. S. & CHAKRABORTY, D. 2013 Effect of side confining walls on the growth rate of compressible mixing layers. *Comput. Fluids* **86**, 500–509.

JIMÉNEZ, J. 2004 *Turbulence and Vortex Dynamics*. Notes for the Polytechnic Course on Turbulence. École Polytechnique, Paris.

KIDA, S. & ORSZAG, S. A. 1990 Energy and spectral dynamics in forced compressible turbulence. *J. Sci. Comput.* **5**, 85–125.

KIDA, S. & ORSZAG, S. A. 1992 Energy and spectral dynamics in decaying compressible turbulence. *J. Sci. Comput.* **7**, 1–34.

KOMPERDA, J., GHIASI, Z., LI, D., PEYVAN, A., JABERI, F. & MASHAYEK, F. 2020a A hybrid discontinuous spectral element method and filtered mass density function solver for turbulent reacting flows. *Numer. Heat Transfer* **78**, 1–29.

KOMPERDA, J., LI, D., PEYVAN, A. & MASHAYEK, F. 2020b Filtered density function for shocked compressible flows on unstructured spectral element grids. *AIAA Paper* 2020-1789.

KOOCHESFAHANI, M. M., CATHERASOO, C. J., DIMOTAKIS, P. E., GHARIB, M. & LANG, D. B. 1979 Two-point LDV measurements in a plane mixing layer. *AIAA J.* **17**, 1347–11351.

KOPRIVA, D. A. 1998 A staggered-grid multidomain spectral method for the compressible Navier–Stokes equations. *J. Comput. Phys.* **143**, 125–158.

KOPRIVA, D. A. & KOLIAS, J. H. 1996 A conservative staggerd-grid Chebyshev multidomain method for compressible flows. *J. Comput. Phys.* **125**, 244–261.

KOVASZNAY, L. S. G. 1953 Turbulence in supersonic flow. *J. Aeronaut. Sci.* **20**, 657–682.

KRAMER, W., BUTLER, M., BAUER, G., CHADALAVADA, K. & MENDES, C. 2015 Blue waters parallel I/O storage sub-system. In *High Performance Parallel I/O*, pp. 17–32. CRC Publications, Taylor and Francis Group.

LAIZET, S. & LAMBALLAIS, E. 2006 *Direct Numerical Simulation of a Spatially Evolving Flow from an Asymmetric Wake to a Mixing Layer*. Springer.

LAIZET, S., LARDEAU, S. & LAMBALLAIS, E. 2010 Direct numerical simulation of a mixing layer downstream a thick splitter plate. *Phys. Fluids* **22**, 015104.

LANDAHL, M. T. & MOLLO-CHRISTENSEN, E. 1992 *Turbulence and Random Processes in Fluid Mechanics*, 2nd edn. Cambridge University Press.

LELE, S. K. 1994 Compressibility effects on turbulence. *Annu. Rev. Fluid Mech.* **26**, 211–254.

LI, D., GHIASI, Z., KOMPERDA, J. & MASHAYEK, F. 2016 The effect of inflow Mach number on the reattachment in subsonic flow over a backward-facing step. *AIAA Paper* 2016-2077.

LI, D., KOMPERDA, J., GHIASI, Z., PEYVAN, A. & MASHAYEK, F. 2019 Compressibility effects on the transition to turbulence in spatially developing plane free shear layer. *Theor. Comput. Fluid Dyn.* **33**, 577–602.

LIU, H., WANG, B., GUO, Y., ZHANG, H. & LIN, W. 2013 Effects of inflow Mach number and step height on supersonic flows over a backward-facing step. *Adv. Mech. Engng* **2013**, 0–11.

LIVESCU, D., JABERI, F. A. & MADNIA, C. K. 2002 The effects of heat release on the energy exchange in reacting turbulent shear flow. *J. Fluid Mech.* **450**, 35–66.

LUI, C. & LELE, S. 2001 Direct numerical simulation of spatially developing, compressible, turbulent mixing layers. *AIAA Paper* 2001-291.

MATHEW, J. & BASU, A. J. 2002 Some characteristics of entrainment at a cylindrical turbulence boundary. *Phys. Fluids* **14** (7), 2065–2072.

MCMULLAN, W. A., GAO, S. & COATS, C. M. 2009 The effect of inflow conditions on the transition to turbulence in large eddy simulations of spatially developing mixing layers. *Intl J. Heat Fluid Flow* **30**, 1054–1066.

MITTAL, A. & GIRIMAJI, S. S. 2019 Mathematical framework for analysis of internal energy dynamics and spectral distribution in compressible turbulent flows. *Phys. Rev. Fluids* **4**, 042601.

MONKEWITZ, P. A. & HEURRE, P. 1982 Influence of the velocity ratio on the spatial instability of mixing layers. *Phys. Fluids* **25**, 1137–1143.

MOSER, R. D. & ROGERS, M. M. 1993 The three-dimensional evolution of a plane mixing layer: pairing and transition to turbulence. *J. Fluid Mech.* **247**, 275–320.

OLSEN, M. G. & DUTTON, J. C. 2003 Planar velocity measurements in a weakly compressible mixing layer. *J. Fluid Mech.* **486**, 51–77.

PANTANO, C. & SARKAR, S. 2002 A study of compressibility effects in the high-speed turbulent shear layer using direct simulation. *J. Fluid Mech.* **451**, 329–371.

PAPAMOSCHOU, D. & ROSHKO, A. 1988 The compressible turbulent shear layer: an experimental study. *J. Fluid Mech.* **197**, 453–477.

PASSOT, T. & POUQUET, A. 1987 Numerical simulation of compressible homogeneous flows in the turbulent regime. *J. Fluid Mech.* **181**, 441–466.

PICKETT, L. M. & GHANDHI, J. B. 2002 Passive scalar mixing in a planar shear layer with laminar and turbulent inlet conditions. *Phys. Fluids* **14** (3), 985.

PIERREHUMBERT, R. T. & WIDNALL, S. E. 1982 The two and three dimensional instabilities of a spatially periodic shear layer. *J. Fluid Mech.* **114**, 59–82.

PIROZZOLI, S., BERNARDINI, M., MARIÉ, S. & GRASSO, F. 2015 Early evolution of the compressible mixing layer issued from two turbulent streams. *J. Fluid Mech.* **777**, 196–218.

POINSOT, T. J. & LELE, S. K. 1992 Boundary-conditions for direct simulations of compressible viscous flows. *J. Comput. Phys.* **101**, 104–129.

POPE, S. B. 2000 *Turbulent Flows*. Cambridge University Press.

ROGERS, M. M. & MOSER, R. D. 1992 The three-dimensional evolution of a plane mixing layer: the Kelvin–Helmholtz rollup. *J. Fluid Mech.* **243**, 183–226.

ROGERS, M. M. & MOSER, R. D. 1994 Direct simulation of a self-similar turbulent mixing layer. *Phys. Fluids* **6**, 903–923.

SANDHAM, N. D. 1989 A numerical investigation of the compressible mixing layer. PhD thesis, Stanford University, Stanford, CA.

SANDHAM, N. D. & REYNOLDS, W. C. 1990 Compressible mixing layer: linear theory and direct simulation. *AIAA J.* **28**, 618–624.

SANDHAM, N. D. & REYNOLDS, W. C. 1991 Three-dimensional simulations of large eddies in the compressible mixing layer. *J. Fluid Mech.* **224**, 133–158.

SANDHAM, N. D. & SANDBERG, R. D. 2009 Direct numerical simulation of the early development of a turbulent mixing layer downstream of a splitter plate. *J. Turbul.* **10**, 1–17.

SARKAR, S. 1995 The stabilizing effect of compressibility in turbulent shear flow. *J. Fluid Mech.* **282**, 163–186.

SARKAR, S., ERLEBACHER, G. & HUSSAINI, M. Y. 1991a Direct simulation of compressible turbulence in a shear flow. *Theor. Comput. Fluid Dyn.* **2**, 291–305.

SARKAR, S., ERLEBACHER, G., HUSSAINI, M. Y. & KREISS, H. O. 1991b The analysis and modelling of dilatational terms in compressible turbulence. *J. Fluid Mech.* **227**, 473–493.

SARKAR, S. & LAKSHMANAN, B. 1991 Application of a Reynolds stress turbulence model to the compressible shear layer. *AIAA J.* **29**, 743–49.

SHARMA, A., BHASKARAN, R. & LELE, S. K. 2011 Large-eddy simulation of supersonic, turbulent mixing layers downstream of a splitter plate. *AIAA Paper* 2011-208.

SIMONE, A., COLEMAN, G. N. & CAMBON, C. 1997 The effect of compressibility on turbulent shear flow: a rapid-distortion-theory and direct-numerical-simulation study. *J. Fluid Mech.* **330**, 307–338.

TENNEKES, H. & LUMLEY, J. L. 1972 *A First Course in Turbulence*. MIT Press.

THOMPSON, K. W. 1987 Time dependent boundary conditions for hyperbolic systems. *J. Comput. Phys.* **68**, 1–24.

THOMPSON, K. W. 1990 Time dependent boundary conditions for hyperbolic systems 2. *J. Comput. Phys.* **89**, 439–461.

VREMAN, A. W., SANDHAM, N. D. & LUO, K. H. 1996 Compressible mixing layer growth rate and turbulence characteristics. *J. Fluid Mech.* **320**, 235–258.

WANG, B., WEI, W., ZHANG, Y., ZHANG, H. & XUE, S. 2015 Passive scalar mixing in $M_c < 1$ planar shear layer flows. *Comput. Fluids* **123**, 32–43.

ZEMAN, O. 1990 Dilatation dissipation: the concept and application in modeling compressible mixing layers. *Phys. Fluids* A **2**, 178–188.

ZHANG, D., TAN, J. & YAO, X. 2019 Direct numerical simulation of spatially developing highly compressible mixing layer: structural evolution and turbulent statistics. *Phys. Fluids* **31**, 036102.

ZHOU, Q., HE, F. & SHEN, M. Y. 2012 Direct numerical simulation of a spatially developing compressible plane mixing layer: flow structures and mean flow properties. *J. Fluid Mech.* **711**, 437–468.